Report Title

Development of Flexible Extremities Protection utilizing Shear Thickening Fluid/Fabric Composites

ABSTRACT

ABSTRACT

A systematic approach was undertaken to enhance spike resistance of flexible body armor. A traditional STF composite is consisted of fumed silica particles (about 7 nm in diameter but highly agglomerated due to van der Waals forces), PEG, and Kevlar. PEG is added to an aqueous suspension of silica and the solution is evaporated to remove water. This process of adding PEG to silica suspension and evaporation is continued several times until the concentration of silica to PEG comes around 55:45 by weight. At this ratio, the mixture is usually termed as Shear Thickening Fluid (STF) since it shows a sudden spike in viscosity at a certain shear rate when tested in a Rheometer. This sudden rise in viscosity is due to hydroclustering of silica particles within the carrier fluid, PEG. Such hydroclustering requires some movement and orientation of particles which is only possible when the carrier fluid is in liquid or in semi-liquid condition. Once STF is impregnated with Kevlar (with the help of ethanol, and subsequently dried) movement of silica particles are restricted further. Chances of hydroclustering and any alignment of particles to provide an instantaneous rise in viscosity and offer resistance to spike penetration are remote. It is therefore believed that under dry condition, resistance to spike penetration mostly comes from the energy required to (i) separate the filaments in fiber tows, (ii) deform the fiber, which is directly related to the elastic energy of the fiber, and (iii) plow through the particle-polymer-fiber layers – which is related to frictional energy. We believe, a considerable amount of energy is absorbed by steps (i) and (iii). Energy absorption in these two steps can be increased if we can increase the bonding between the three components; particle, polymer, and fiber. We cannot do much with the fiber deformation and fracture (step-ii) until its elastic energy and cut properties are improved. We focused on increasing the chemical bonding. Following steps were taken:

Size of the silica particles was increased to 30 nm to reduce agglomerations. These particles were then functionalized with a silane coupling agent to develop a bonding with PEG. This helped develop a Si-O-Si (siloxane) bond as evidenced in the FTIR spectra of silated silica. SEM pictures also showed that particles are highly clustered around the filament after functionalization. After functionalization of particles, spike resistance increased to 40 J-cm2/g. With regular STF composite, this value was around 15-20 J-cm2/g.

Since particles were treated with silane during functionalization, it was decided to remove PEG from the system and simplify the procedure. The objective was to increase bonding between particle and polymer which could be maintained without having PEG in there. However, the ratio of particle to polymer remained as before since we needed enough silica for frictional energy. NIJ tests indicated a spike resistance of 45 J-cm2/g, i.e., we did not loose any spike resistance.

Next, we attempted to develop a bonding between particle, polymer and Kevlar fiber. Treatment of silica particles with silane installs an amino functional group (N-H) on the surface of the silica particles. On the other hand, Kevlar also has an N-H (amide) functional group in its repeating amide group. Formaldehyde is an ideal tool to connect such pairs of amine. We decided to include Glutaraldehyde (Gluta) in our system. Use of this cross-linking fixative polymer (Gluta) allowed formation of three distinct bonds; C-N bonding, C-H band, and C-C stretch which were evidenced by FTIR spectra. These bonds were identified by their absorption frequencies. With the addition of Gluta, the peak for each of the three bonds increased indicating that the total number of bonds (i.e., cross-linking density) has increased. Such higher concentrations of chemical bonds allowed silica particles to bond much more intensely with the polymer and the Kevlar fiber. Spike resistance of this system was phenomenal – 220 J-cm2/g, almost 10 times more than that of regular STF-Kevlar system – an unprecedented materials property for flexible armor was achieved.

Enter List of papers submitted or published that acknowledge ARO support from the start of the project to the date of this printing. List the papers, including journal references, in the following categories:

(a) Papers published in peer-reviewed journals (N/A for none)

Number of Papers published in non peer-reviewed journals:

(c) Presentations

1.J. Mayo, Jr., A. Lewis, M. V. Hosur, S. Jeelani, "Cut Studies of Brittle and Ductile Fibers," SAMPE 2009 Conference, Baltimore, MD, May 2009

2.Vijaya K. Rangari, Tarig Hassan and Shaik Jeelani, "Synthesis and Mechanical Properties of Shear Thickening Fluid/Kevlar Composite for Body Armor Application," SAMPEE-2008, May 16-21, Long Beach, CA.

3.Hassan Mahfuz, Vincent Lambert, Patrick Bordner, and Vijaya Rangari, "Improving Stab Resistance of Flexible Body Armor using Silane Coupling Agents and Cross-linking Fixatives with Silica Nanoparticles," invited presentation at the 2008 ASME International Mechanical Engineering Congress and Exhibition (IMECE), Boston, MA, Oct. 31 – Nov. 6, 2008.

4.Mahfuz, H., Clements, F. and Justin, S., "Functionalization of Silica Nanoparticles to Improve Stab Resistance of Kevlar Fabrics," SES 2006, University Park, PA, August 13-16, 2006.

5.Mahfuz, H., Lambert, V. and Bordner, P., "Improving Stab Resistance of Flexible Body Armor using Silane Coupling Agent and Cross-Linking Fixatives with Silica Nanoparticles," ASME International Mechanical Engineering Congress and Exposition, October 31 – November 6, 2008, Boston, Massachusetts, Presented at the Conference.

6.International Congress on Rheology 2008, 8/5/2008, Effects of particle hardness on shear thickening colloidal suspension rheology, University of Konstanz, Germany, Department of Physics, 7/4/2008 (invited lecture), Microstructure of Shear Thickening Colloidal Dispersions: "STF Armor"- Nanoparticle Composites for Flexible Ballistic Materials.

7.SoftMatt-2008, 6/19/2008, – Micromechanics of concentrated, near hard-sphere suspensions (poster) 7.ACS Colloid and Surface Science Symposium,

8.NCSU, 6/16/2008 – Particle Hardness Effects on Concentrated Colloidal Suspension

9.Rheology, ACS Colloid and Surface Science Symposium, NSCU, 6/16/2008- The influence of Interparticle Interactions and Hydrodynamic Forces on Shear Thickening in Concentrated Colloidal Dispersions and Slurries

10.Chemical Engineering, UC Santa Barbara, CA, May, 2008 (invited lecture)- The Rheology Of Colloidal & Nanoparticle Dispersions: "Stf Armor™"- Nanoparticle Composites For Flexible Ballistic Materials.

11.Chemical Engineering, Purdue Univ. Indiana, Feb. 2008 (invited lecture) – The Rheology Of Colloidal & Nanoparticle Dispersions: "Stf Armor™"- Nanoparticle Composites For Flexible Ballistic Materials.

12.Chemical Engineering, UC Riverside, CA, Feb. 2008 (invited lecture) – The Rheology Of Colloidal & Nanoparticle Dispersions: "Stf Armor™"- Nanoparticle Composites For Flexible Ballistic Materials.

13.Rheophysics, ESCPI Paris, France, Jan. 2008- Shear-induced organization in colloidal dispersions: The hydrocluster microstructure in shear thickened colloidal suspensions

14."Investigating the High Strain Rate Compression Shear Behavior of a Discontinuous Shear-Thickening Fluid (STF)." 1st place award in the 21st Annual Technical Conference of the American Society for Composites Student poster competition.

15."Implementing the Split-Hopkinson Pressure Bar Technique for Viscous Fluid Evaluation." 1st place award in the 53rd International SAMPE Symposium and Exhibition, Long Beach CA, May 2008.

16. Sreedhar Poluchalla, Mahesh V. Hosur, Shaik Jeelani, "Investigations on the Stab Resistance of Kevlar Fabrics Impregnated with Shear Thickening Fluid," ASME International Mechanical Engineering Congress and Exposition, 15 November 2007, Seattle, WA

Number of Presentations: 1.00

Non Peer-Reviewed Conference Proceeding publications (other than abstracts):

Received Paper

TOTAL:

Number of Non Peer-Reviewed Conference Proceeding publications (other than abstracts):

Peer-Reviewed Conference Proceeding publications (other than abstracts):

Number of Manuscripts:

Books

Received Paper

TOTAL:

Patents Submitted

Patents Awarded

Awards

1. Shaik Jeelani: 2011 Presidential Award for Mentoship - presented by President Obama at the White House on December 12, 2011.

2. Mahesh Hosur: 2009-2010 Faculty Performance Award for Research in the College of Engineering, Architecture and Physical Sciences.
Mahesh Hosur: Nominated by the College of Engineering for the Tuskegee University Faculty Achievement Award in Spring 2011.

3. Hassan Mahfuz: Researcher of the Year (FAU), 2008

4. Hassan Mahfuz: Elected Fellow of ASME, December 2010

5. Amanda Lim, 1st place award in the 21st Annual Technical Conference for the American Society for Composites, Student Poster Competition

6. Amanda Lim - 2nd place award at the 2007 SBaltimore-Washington SAMPE, Student Nite Competition

7. Amanda Lim - 1st place award in the 53rd International SAMPE Symposium and Exhibition, Long Beach, CA, May 2008

8. Amanda Lim - 1st place award in the 11th International Congress of the SEM Student Paper Symposium, Orlando, FL, June 2008

Graduate Students

NAME	PERCENT_SUPPORTED	Discipline
Andre Lewis	0.50	Mechanical Engineering
Shifra Burton	0.50	Chemical Engineering
Patrick Bordner	0.50	Ocean Engineering
DeAnna Sewell	0.50	Ocean Engineering
Jarmarius Keith	0.50	Mechanical Engineering
Joe Houghton	0.50	Mechanical Engineering
Emory Head	0.50	Mechanical Engineering
Keosha Forest	0.50	Mechanical Engineering
Brian Rosen	0.50	Materials Engineering
Monica Tubbs	0.50	Mechanical Engineering
Benjamin Schiffman	0.50	Chemical Engineering
Josh Schein	0.50	Chemical Engineering
Shanise Hudley	0.50	Mechanical Engineering
James McGovern	0.50	Mechanical Engineering
Amir Usher	0.50	Mechanical Engineering
Joe Houghton	0.50	Mechanical Engineering
Bryan Clayton	0.50	Mechanical Engineering
Chris Miller	0.50	Mechanical Engineering
FTE Equivalent:	**9.00**	
Total Number:	**18**	

Student Metrics

This section only applies to graduating undergraduates supported by this agreement in this reporting period

The number of undergraduates funded by this agreement who graduated during this period:	18.00
The number of undergraduates funded by this agreement who graduated during this period with a degree in science, mathematics, engineering, or technology fields:	18.00
The number of undergraduates funded by your agreement who graduated during this period and will continue to pursue a graduate or Ph.D. degree in science, mathematics, engineering, or technology fields:	10.00
Number of graduating undergraduates who achieved a 3.5 GPA to 4.0 (4.0 max scale):	8.00
Number of graduating undergraduates funded by a DoD funded Center of Excellence grant for Education, Research and Engineering:	8.00
The number of undergraduates funded by your agreement who graduated during this period and intend to work for the Department of Defense	13.00
The number of undergraduates funded by your agreement who graduated during this period and will receive scholarships or fellowships for further studies in science, mathematics, engineering or technology fields:	10.00

Names of Personnel receiving masters degrees

NAME
Jessie B. Mayo Jr.
Harish Rao
Sreedhar Poluchalla
Floria Clements
Vincent Lambert
Tarig Hasan
James Manimala
Total Number: 7

Names of personnel receiving PHDs

Most significant accomplishments are as follows:

•A systematic study has been conducted to understand the cut and fracture behavior of various types of commercial fibers for potential application to flexible armor. Unique testing facilities have been developed at ARL to conduct these experiments. This component of the project has demonstrated an overwhelming amount of collaboration between Tuskegee University and ARL.

•It has been demonstrated that ultrahigh molecular weight polyethylene (UHMWPE) based fibers such as Spectra and Dyneema has superior cut resistance than that of Kevlar. The study also showed that S-glass fiber has very good potential for armor application. But further studies are needed to confirm this finding.

•A sonochemical procedure has been introduced to produce shear thickening fluid (STF) in large quantities. The procedure uses silica nanopowder dispersed into polyethylene glycol (PEG) using high frequency ultrasonic waves in presence of a solution. Large amount of solution and high intensity of irradiation allows uniform distribution of nanoparticles in the polymer.

•NIJ tests have demonstrated that Spectra provides more stab resistance than Kevlar as it was concluded in the cut and fracture studies. Multiple soaking of the fabric with silica-silane-Gluta solution have shown that knife resistance can be enhanced almost 3 times; from 6 J-cm2/g to 20 J-cm3 /g for zero-layer penetration.

•Micro droplet tests have indicated that dynamic friction at the fiber/matrix interface was responsible for such enhancement in knife resistance.

•A comprehensive study on the high strain rate behavior of STF has been completed. Complex relationship between particle volume fraction, strain rate, and onset of shear thickening has been deduced through mathematical formulations, and later validated through Hopkinson bar experiments.

•A two dimensional homogenized continuum model has been developed to characterize the non-linear anisotropic material properties of the neat and nanoparticle-impregnated fabrics under large deformation. Validation of the model was performed by simulating a 300 off-axis tension test and a static indentation test.

Technology Transfer

Figure 1b shows the general behavior of high performance fibers during cut resistance testing at 45° longitudinal incidence with a Celanese food processing blade. At this fiber angle, Vectran has the highest cut resistance force with Twaron being very close in magnitude. Zylon has the lowest magnitude of all of the fibers tested. As the fiber angle changed from 0° to 45° the response of some of the fibers became more noisy.

Figure 1c shows the general behavior of high performance fibers during cut resistance testing at 45° transverse incidence with a Celanese food processing blade. At this blade angle, Dyneema has the highest cut resistance force and S-glass has the lowest cut resistance force.

2. Size effects and scaling

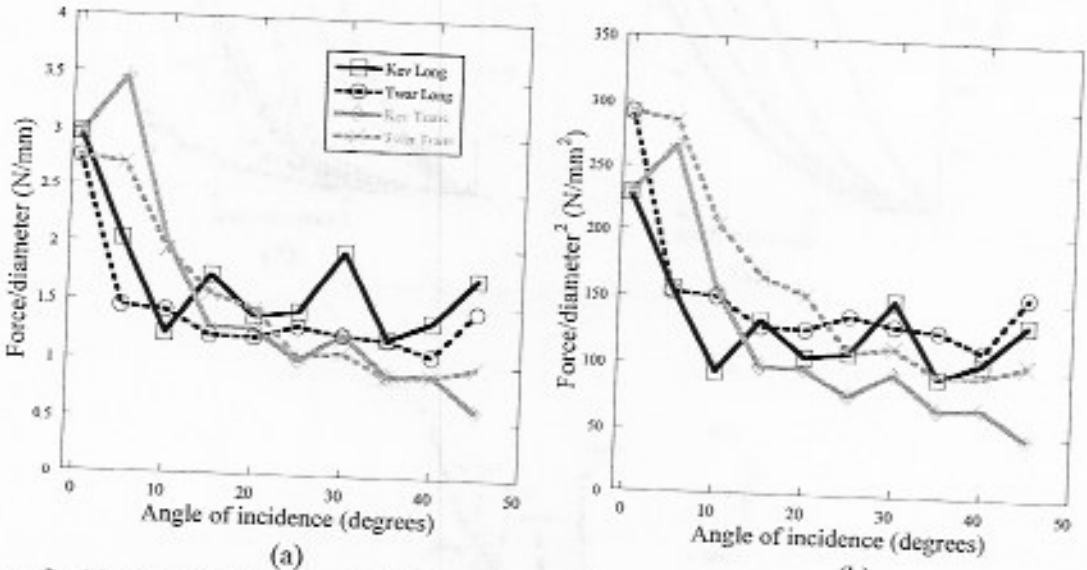


Figure 3. (a) Force/diameter and (b) force/diameter^2 as a function of angle of incidence for Kevlar and Twaron fiber cut with Celanese blade.

This section compares Kevlar and Twaron. In this section, the reasons for the force/diameter designation are discussed. It is most reasonable to normalize by the fiber diameter instead of diameter^2 because it is envisioned that the blade-fiber contact was a line contact rather than a cross-sectional area loading. Alternatively, one could choose to normalize the cutting force by the fiber cross-sectional area, proportional to fiber diameter squared. To begin, once the Kevlar and Twaron cut resistance data is normalized by either the diameter or diameter^2; the plots with the closest comparable data will determine the correct normalization scheme.

Figure 3a and 3b show the force/diameter and force/diameter^2 as a function of angle of incidence for Kevlar and Twaron. The plots contain both longitudinal and transverse cut resistance results. There is a greater amount of overlap with force/diameter plot than with force/diameter^2 plot. F/d is chosen for normalization of the fibers.

a study was done in order to develop a test procedure that reliably and reproducibly measures the cutting resistance of yarns under tension-shear conditions. Further studies by Shin and Shockey would expand the study to Kevlar and Spectra (2006). A very limited amount of single fiber cut studies have been conducted. Knoff (2001) investigated the fiber transverse deformation work and cut performance of protective apparel.

Mechanical characterization of single fibers is a study that has been conducted by many. Hearle et al. (1969) studied the theory of tensile mechanics of staple fiber yarns. Liu et al. (2007) examined the tensile properties of electrospun multi-walled nanofibers. The dynamic tensile response of aged Zylon (PBO) was examined by Rhorer et al. (2007). Transverse compression testing was studied by Cheng et al. (2004) and Singletary (2000). Forster et al. (2006) examined the effect of bending on Zylon fibers. Very few mechanistic studies have been conducted on single fibers. Single fiber studies, which are more fundamental that fabric and yarn studies, are necessary to fortify and improve several types of materials.

The scope of the current study is to explore the relationship between fiber type on cut resistance and the implications for the design and performance of stab resistant body armor, to provide comprehension of how fiber structure influence cut behavior, and to understand on a fundamental level, the physics/mechanics of cut behavior.

II. Experimental

The fibers that were examined are in Table 1.

Table 1. Fibers examined in cut resistance study.

Trade Name	Chemical Composition	Denier	Diameter	Strain to failure (%)	Density (g/cm^3)	Modulus (GPa)	Tensile Strength (GPa)
Kevlar 129	aramid	840	13	3.3	1.44	96	3.38
Twaron	aramid	840	9.46	3.3	1.44	96	3.38
Dyneema SK-76	UHMWPE	400	18.8	3.6	0.98	88	2.62
Zylon (PBO)	aromatic heterocyclic	500	12.3	3.5	1.54	180	5.8
Vectran	aromatic polyester	1500	23.5	3.3	1.41	75	3.2
Technora	aramid	1500	12.3	4.6	1.39	73	3.44
S2-glass	glass	2980	9.29	5.5	2.48	85	4.8
Carbon fiber	graphite	800	8	2	1.8	234	4.83

Kevlar and Twaron have identical molecular structures and scientific name (poly-paraphenylene terephthalamide). One major difference between the two high performance fibers is their diameter. The diameters of these fibers as observed by the author through scanning electron microscopy were 13.0 μm and 9.46 μm for Kevlar and Twaron, respectively.

These fibers were held in place with a specially designed fiber clamp that is shown in Fig. 1. The fiber clamp fixture has a rotary platform, angle indicator, and rubber clamps. The two rubber clamps on the fixture were 127 mm apart, which gave the fiber to be investigated a gage length of 127 mm. The fiber was clamped at one end and at a position of 127 mm at that end. A Celanese food processing blade (American Cutting Edge, Inc., Centerville, OH) was mounted in

Here x is the half of the length of the fiber (63.5 mm), y is the extension or displacement of the fiber at failure, and r is the half length of the fiber at failure. Thusly, the formula used to determine the cut strain to failure is

$$\varepsilon_c = \frac{l_f - l_o}{l_f}.$$

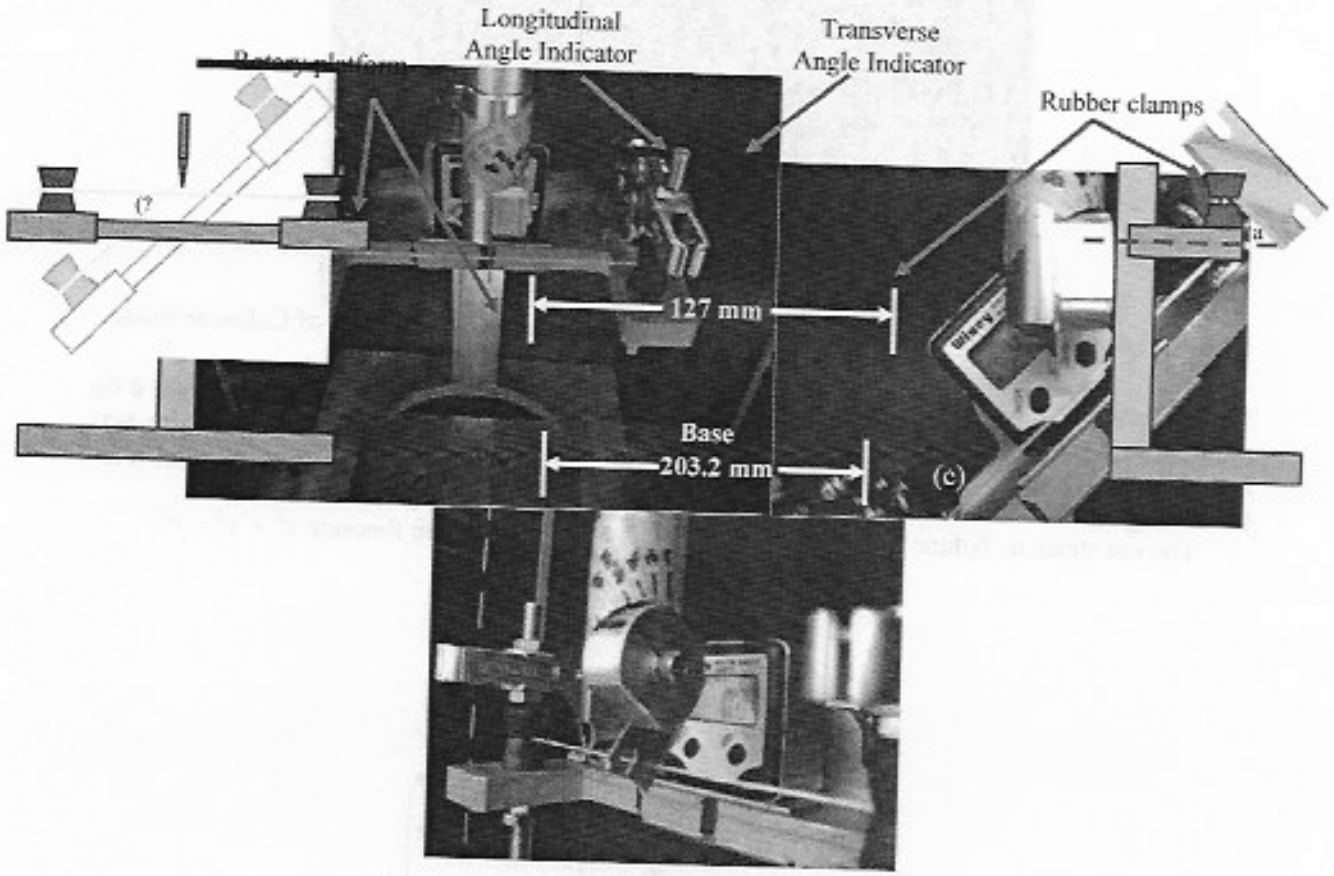


Figure 2. Photographs of (a) fiber clamp fixture showing normal incidence cut resistance testing, (b) longitudinal incidence, (c) transverse incidence, and (d) normal incidence cut resistance testing.

The effect of cutting angle on cut performance was evaluated through two arrangements; longitudinal (Fig. 2b) and transverse (Fig. 2c). The numbering convention θ-α was used to refer to the longitudinal-transverse cut angles for a given experiment. All fibers were cut at longitudinal angles and transverse angles varying from 0° to 45° in 5° increments. Longitudinal cut testing involved varying the angle of the fiber under investigation while keeping the blade at $\alpha = 0°$, and transverse cut testing involved varying the angle of blade while keeping the fiber at $\theta = 0°$. All of the fibers listed in table 1 were tested for cut resistance.

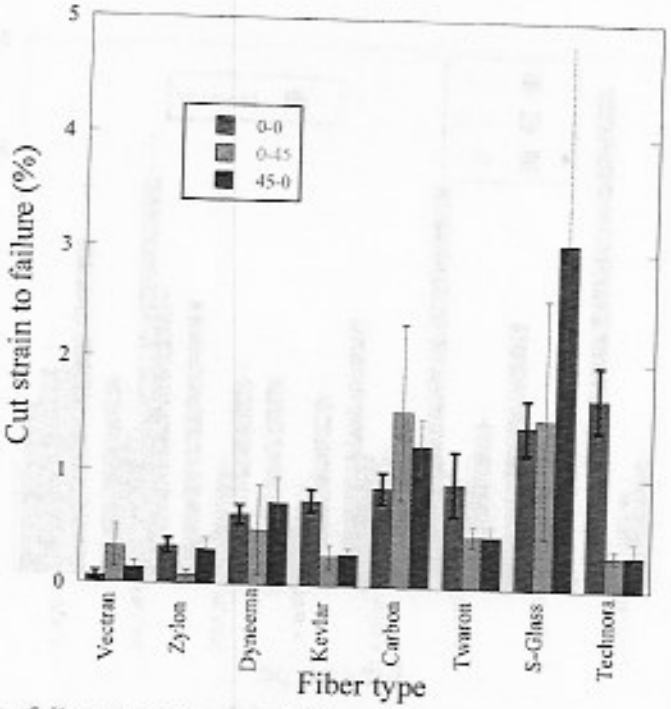


Figure 5. Cut strain to failure as a function of fiber type for all fibers tested for cut resistance at normal incidence, 45° longitudinal degrees, and 45° transverse degrees.

3. Cut Strain to Failure Results

Figure 5 shows the cut strain to failure as a function of fiber type of the fibers examined in the cut resistance study. At normal incidence (0-0), Vectran had the lowest cut strain to failure while Technora has the highest. At 45 longitudinal degrees (0-45), Zylon had the lowest cut strain to failure while Carbon had the highest cut strain to failure. At 45 transverse degrees (45-0), Vectran had the lowest cut strain to failure while S-glass had the highest. Errorwise, S-glass had significant errors for angled testing.

4. Organic fiber results

In general, as the fiber angle increased, the organic fibers cut resistance decreased in the lower angles but began to level out for the duration of the testing. As the blade angle increased, the organic fibers cut resistance decreased. On average, considering all angles tested; Zylon had the highest cut resistance and Vectran had the lowest out of the organic fibers. Vectran and Technora average cut resistances were very close in magnitude with Kevlar cut resistance not far behind. Twaron had the lowest cut resistance of the tested organic fibers.

Table 2. Summary of average force/diameter (N/mm) of longitudinal cut resistance testing.

Fiber	0-0	0-5	0-10	0-15	0-20	0-25	0-30	0-35	0-40	0-45	Average
Kevlar	2.97	2.03	1.22	1.73	1.38	1.43	1.95	1.21	1.36	1.74	1.70
Twaron	2.76	1.45	1.42	1.21	1.20	1.30	1.23	1.20	1.07	1.46	1.43

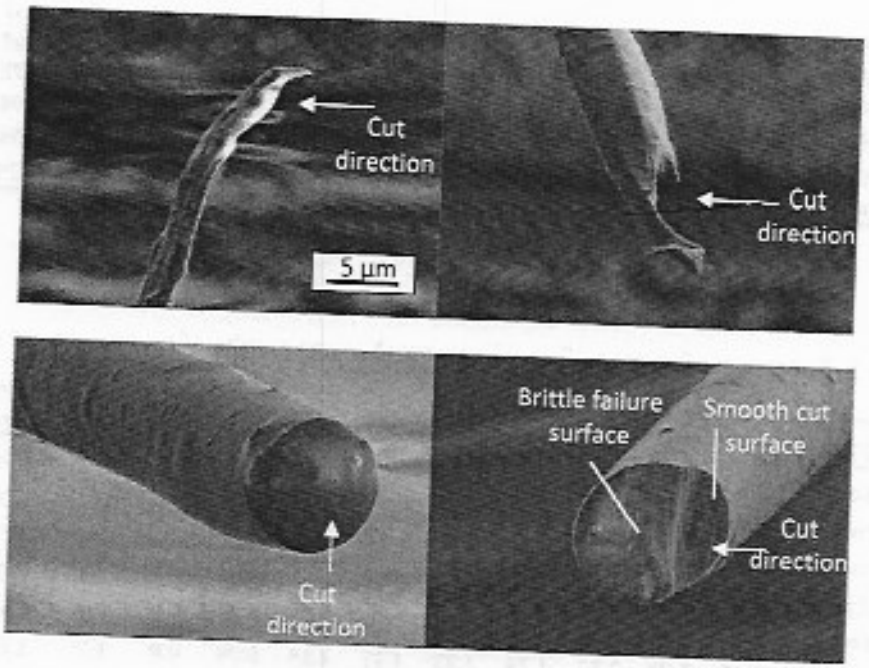


Figure 7. SEMs of (top) Kevlar and (bottom) S-glass fibers after cut resistance testing at normal incidence.

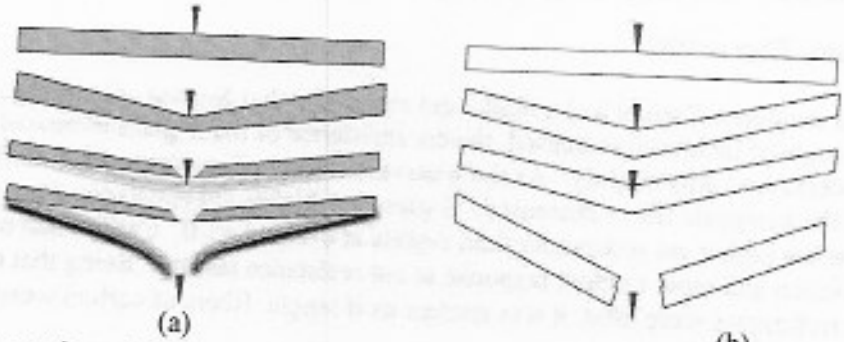


Figure 8. Schematics of failure dynamics and responses of (a) Kevlar and (b) S-glass fibers during cut resistance testing.

Figure 7 shows the SEMs of the surface damage of the Kevlar and S-glass fibers after cut resistance testing. Figure 8 is the failure progression inferred from the SEMs of the two fibers. The blade pressed into the Kevlar deforming (crushing) the fiber at the point of incident. The blade cut between halfway to three quarter through the fiber until there is interfibril splitting created by the fibrils of the Kevlar fiber. The fibrils are too strong to be cut to because of increasing transverse compression, the fibrils finally give way due to tension instead of cutting. The blade pressed into the S-glass but no deformation could be observed. Instead, the blade pressed a dent into the S-glass and with increasing transverse compression, the S-glass fiber broke with brittle failure. With S-glass, a smooth cut surface is seen where the blade enters into the fiber. A rough, brittle fracture zone is seen where the S-glass fiber breaks because of tension.

encompasses a fibril bundle that has to be broken through with tension. This is easily accomplished because of the new reduced cross-sectional area left after the shearing away of the Kevlar layer. More branching of the fibrils are seen in the SEMs of the damaged Kevlar at 45°. With S-glass, the blade makes a similar indentation into the fiber as with normal incidence. There is not much deformation, if any, due to transverse compression. The fiber breaks with brittle failure.

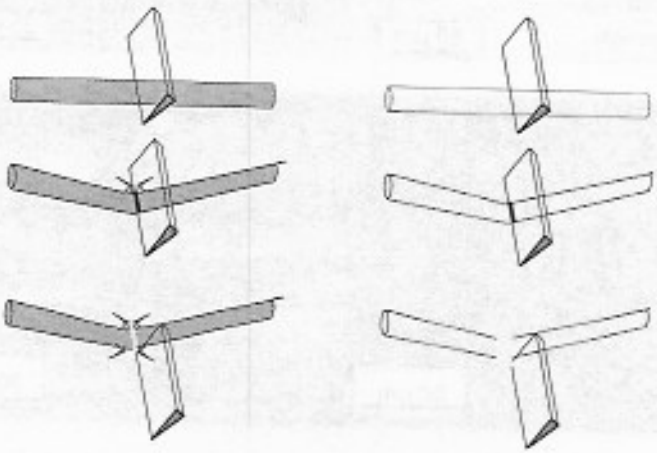


Figure 11. Schematic of failure dynamics and cut response of (a) Kevlar and (b) S-glass fibers after 45° transverse cut testing (45-0).

Figure 11 is the damage progression of the Kevlar and S-glass fiber during 45° transverse cut resistance testing. With Kevlar, the blade shears away material on both sides of the blade as the fiber is being cut. The fiber actually moves up the blade, which creates extra shear. At the conclusion of testing, the outer circumferential layer of the Kevlar fiber has been sheared away (as seen in the SEM). With S-glass, there is no shearing of layers. The blade simply cuts through the S-glass fiber.

IV. Discussion

There is a good amount of deformation seen in ductile (organic fibers). There is very little deformation seen in brittle (inorganic fibers). We see shearing of ductile shell. There is no sort of fiber shearing for brittle fiber. There are well defined brittle and smooth cut surfaces for brittle fiber but no well defined cut surfaces for ductile fiber.

Because of processing parameters, the outer circumference of the Kevlar fiber is hard and crystalline. The regions become more amorphous and softer as the regions come closer to the center. Hard structures call fibrils that have diameters around 30-50 nm exist in the outer shell of the Kevlar fiber (Singletary, 2000). S-glass is a completely amorphous and isotropic fiber. S-glass fiber has a higher hardness than Kevlar fiber. Maximum cut resistance occurs at Kevlar surface. Cut resistance is highest at normal incidence because blade has to break through hard fibril circumference. As angle increases, the circumference is sheared away instead of broken through (less force for shearing away). This explains the pattern for ductile/organic fiber cut

Single filaments of Kevlar fabric have similar damage of single Kevlar fibers (at normal incidence). S-glass has a higher denier, strain to failure, density, and tensile strength than Kevlar fiber. Kevlar has not proven to be an acceptable material for stab armor. From the cut resistance tests in this work, S-glass fiber would be a more acceptable material for stab armor. However, from these tests (single fiber cut resistance tests), we cannot conclude that S-glass would make a suitable material for stab armor. Stab armor has many other parameters that determines its stab resistance (i.e. weave tightness and fiber/mechanism friction, compactness of fabric layers, areal density, etc.). Therefore, actual stab resistance testing, would have to be performed on S-glass armor.

Acknowledgements

David Stepp of the Army Research Office (ARO Battlefield Capability Enhancement (BCE) Program Grant#: W911NF-05-2-0006-P0006).

Army Research Laboratory Staff (Larry Long, Andres Bujanda)

References

Cheng, M. and T. Weerasooriya. 2004. Experimental investigation of the transverse mechanical properties of a single Kevlar KM-2 fiber. *International Journal of Solids and Structures* 41: 6215-6232.

Decker, M.J., C. J. Halbach, C.H. Nam, N.J. Wagner, and E.D. Wetzel. 2007. Stab resistance of shear thickening fluid (STF)-treated fabrics. *Composite Science and Technology* 67 nos. 3-4: 565-579.

Duan, Y., M. Keefe, T. A. Bogetti, and B. Powers. 2006. Finite element modeling of transverse impact on a ballistic fabric. *International Journal of Mechanical Sciences* v48 pgs. 33-43.

Erlich, D. C., D. A. Shockey, and J. W. Simons. 2003. Slow Penetration of Ballistic Fabrics. *Textile Research Journal* 73 no. 2: 179-184.

Forster, A. L., J. W. Chin, and M. Gundlach. 2006. Effect of bending and mechanical damage on the physical properties of poly(p-phenylene-2,6-benzobisoxazole)(PBO) fiber. *Abstracts of Papers of the American Chemical Society*, v231: pg. 274.

Hearle, J. W. S., P. Grosberg, and S. Backer. 1969. Structural Mechanics of Fibers, Yarns, and Fabrics v1.

Knoff, W., August 7-9, 1992. The Effect of Moisture and Heat Treatment on the Lateral Compressive Properties of Poly(p-phenylene terephthalamide) Fibers. Basic Properties of Fibers and Fiber Assemblies, Performance and Design of New Fibrous Materials: *Proceedings of the 21st Textile Research Symposium*, Fuji Kyouiku Kenshusho (Fuji

Ultrasonics Sonochemistry 17 (2010) 947–952

Contents lists available at ScienceDirect

Ultrasonics Sonochemistry

journal homepage: www.elsevier.com/locate/ultsonch

Sonochemical synthesis and rheological properties of shear thickening silica dispersions

Tarig A. Hassan, Vijaya K. Rangari *, Shaik Jeelani

Materials Science and Engineering, Tuskegee University, Tuskegee, AL 36088, USA

ARTICLE INFO

Article history:
Received 20 August 2009
Received in revised form 3 February 2010
Accepted 3 February 2010
Available online 8 February 2010

Keywords:
Shear thickening fluid
Silica nanoparticles
Sonochemical technique

ABSTRACT

A sonochemical method has been developed to synthesize shear thickening fluid. This shear thickening fluid (STF) is composed of hard silicon dioxide nanoparticles and polyethylene glycol (PEG) liquid polymer. The combination of flow-able and hard components at a particular composition, results a material with remarkable rheological properties that is suitable for liquid body armor applications. In the present study nine types of STF's have been synthesized with two different types of silica nanoparticles (15 nm and 200 nm) and polyethylene glycol at various weight fractions using a high intensity ultrasonic irradiation. The resultant STF samples were tested for their rheological and thermal properties. The advantages and disadvantages of this process have been discussed.

© 2010 Elsevier B.V. All rights reserved.

1. Introduction

Shear thickening is a non-Newtonian flow behavior and defined in the British Standard Rheological Nomenclature as the increase of viscosity with increase in shear rate. This is distinguished from rheopexy which is defined as the increase of viscosity with time while the shear rate in constant [1]. Dilatancy is another term used to describe shear thickening, however, it has been avoided since it usually implies an increase in the volume on deformation, which is not considered in this case [2]. The shear thickening trend can take place in concentrated colloidal suspensions that have been shown to exhibit reversible shear thickening resulting in large, sometimes discontinuous, increases in viscosity above a critical shear rate. In order to explain this behavior, two theories of shear thickening phenomenon were reported: the order–disorder transition [3–7] and the "hydrocluster" mechanism [8–13]. This transition from a flowing liquid to a solid-like material occurs due to the formation and percolation of shear induced transient aggregates, or "hydroclusters", that dramatically increase the viscosity of the fluid. Rheological, rheo-optics and flow-SANS experiments have been demonstrated in support of the hydrocluster mechanism of shear thickening phenomenon [14,15] in addition to computer simulations [16]. It was reported in the literature that shear thickening has been observed for a wide variety of suspensions such as clay–water [17], calcium carbonate–water [18], polystyrene spheres in silicon oil [19], iron particles in carbon tetrachloride [20], titanium dioxide-resin [21], silica-poly propylene glycol [22] and silica-ethylene glycol [23].

Many researchers have reported the synthesis of materials that show shear thickening behavior. Raghavan and Khan stated that suspensions of fumed silica in polypropylene glycol exhibit shear thickening under steady shear and "strain-thickening" under oscillatory shear. He also explained the combination of shear and strain thickening behavior through a clustering mechanism which attributes the thickening phenomena to the presence of temporary, flow-induced clusters. These clusters are being generated by the action of hydrodynamic forces on silica aggregates [22]. Each suspension was made in 60 ml batch by adding the liquid polymer to ~14 nm spherical silica particles and mixed in a blender for approximately 1 min and placed under vacuum for 12 h to get rid of air bubbles. The samples concentrations were varied from 3% to 10% weight basis.

Lately Lee et al. [23] reported the applications of STF in liquid body armor fabrication. They also studied the ballistic impact characteristics of Kevlar woven fabrics impregnated with a colloidal shear thickening fluid. The STF was prepared from 466 nm spherical colloidal silica particles and ethylene glycol. The synthesis procedure started with 3 h of centrifugation for the colloidal solution at 3900 rpm to separate the silica particles from the aqueous-based supernatant. The silica sediment was then crushed using a spatula and re-suspended in ethylene glycol using a vortex mixer. This process was repeated four times in order to minimize the amount of residual aqueous supernatant present within the samples. Ballistic impact results of Kevlar fabrics impregnated with this STF sample showed significant enhancements in ballistic penetration resistance of the STF impregnated fabrics compared to neat Kevlar due to the addition of STF without any loss in material

* Corresponding author. Tel.: +1 334 724 4875; fax: +1 334 724 4224.
E-mail address: rangariv@tuskegee.edu (V.K. Rangari).

1350-4177/$ - see front matter © 2010 Elsevier B.V. All rights reserved.
doi:10.1016/j.ultsonch.2010.02.001

Table 1
As-prepared STF samples.

No.	Synthesis technique	Sample	SiO_2 particles size (nm)	SiO_2 weight fraction (%)	PEG weight fraction (%)
1	Sonochemical method	A	15	55	45
2		B	15	52	48
3		C	15	42	58
4		D	15	40	60
5		E	15	38	62
6		F	200	52	48
7		G	200	48	52
8		H	200	40	60
9	Mechanical mixing method	I	15	40	60

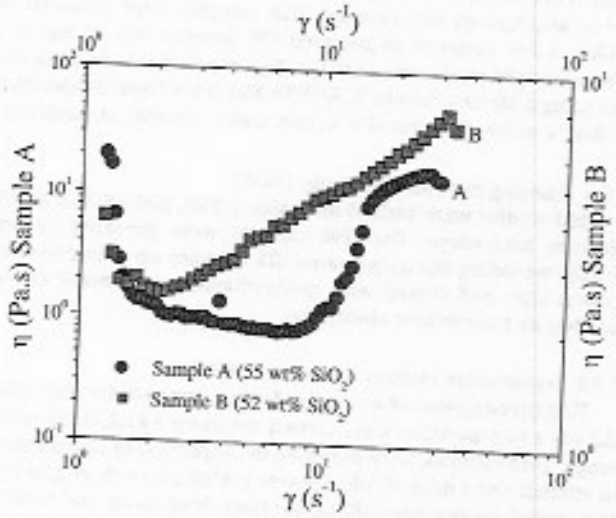


Fig. 1. Rheology graph of STF Sample A and STF Sample B.

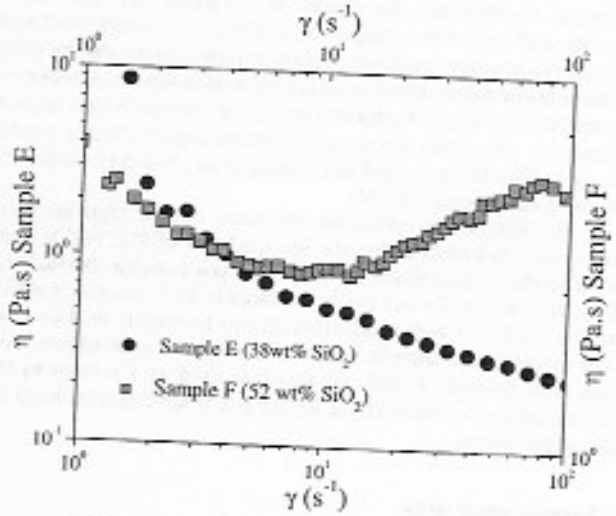


Fig. 3. Rheology graph of STF Sample E and STF Sample F.

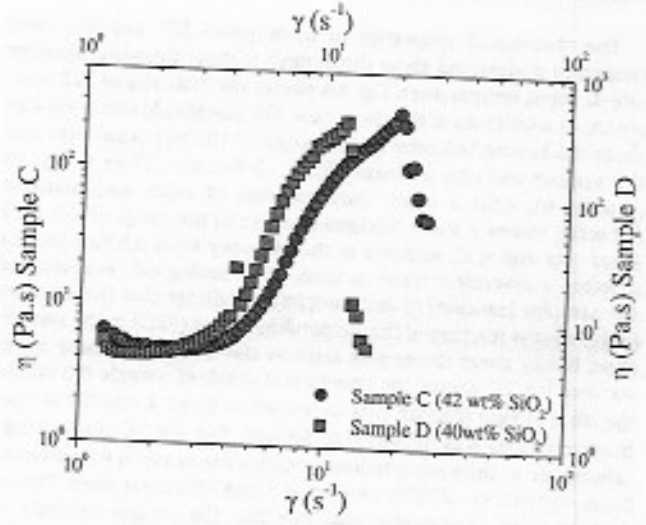


Fig. 2. Rheology graph of STF Sample C and STF Sample D.

is presented in Fig. 3E, and the STF sample (E) contains 62 wt% of PEG and 38 wt% of silica nanopowder. The rheological graph shows that the sample did not exhibit any shear thickening effect, instead, shear thinning behavior is noticeable at shear rate range of ~2–20/s. Among all as-prepared samples, sample (D) shows the best rheological properties. These results suggest that the optimal loading of silica nanoparticles (15 nm) by sonochemical method is 40 wt%.

To study the effect of particles sizes in preparation of STF, a colloidal silica solution (spherical 200 nm) was also used as a source of silica nanoparticles. The sample (F) was prepared using a 52 wt% of silica (200 nm) and 48 wt% of PEG and the rheological graph is presented in Fig. 3F. As seen in the graph the sample viscosity changed from 2 Pa s to around 3.3 Pa s, which is also very low compared to other samples. STF sample (G) contains 48 wt% silica and 52 wt% of PEG and the rheological graph is presented in Fig. 4G. Fig. 4G shows that the sample demonstrates a shear thinning behavior before it starts to exhibit a shear thickening behavior. The viscosity of the sample (G) increases from 4.5 Pa s to 7.5 Pa s, however the shear thickening effect is minimum. STF sample (H) was prepared from 40wt % of silica and 60wt % of PEG. Rheological test results for STF sample (H) are shown in Fig. 4H and it clearly shows the signature of the shear thickening effect and viscosity changes from 2.5 Pa s at shear rate of 3/s to 17 Pa s at about 18.5/s shear rate before a reversal trend is seen. The rheological properties for STF samples (sample (F), sample (G) and sample (H)) confirm that the optimum weight fraction of colloidal silica nanoparticles is 40% to demonstrate better shear thickening behavior. The sudden increase in the viscosity of as-prepared silica dispersions and the shear thickening transition are due to microstructural changes in the fluid along with the hydrocluster mechanism where the formation of particles clusters increases the hydrodynamic stress in the shear thickening fluid that leads to the dramatic increase in the viscosity. From the rheological graphs discussed previously, it is clear that the as-prepared STF samples containing 40 wt% of silica and 60 wt% of PEG shown enhanced shear thickening effect.

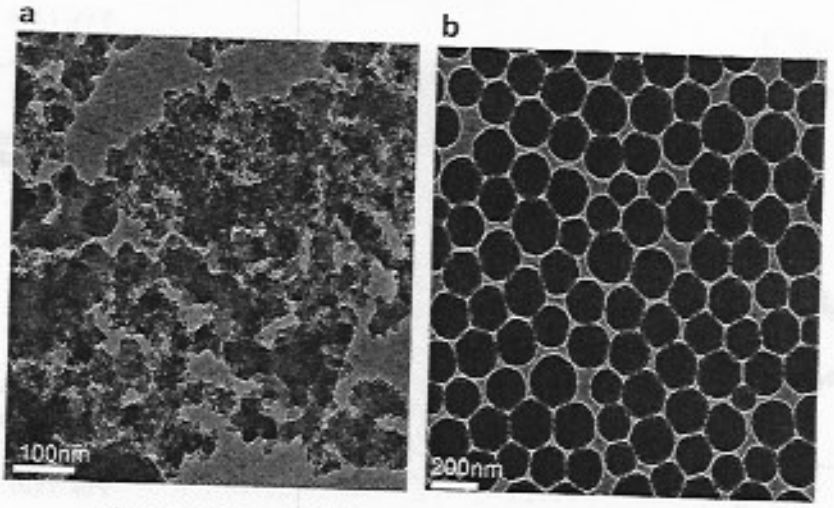


Fig. 9. TEM micrographs for (a) Silica nanoparticles (b) colloidal silica solution.

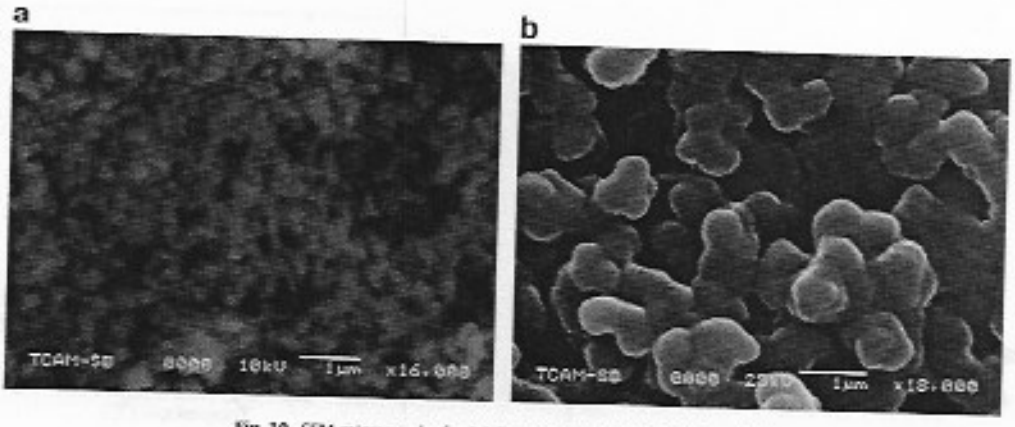


Fig. 10. SEM micrographs for (a) STF sample D and (b) STF Sample H.

Fig. 5 shows a comparison of rheological properties of STF samples prepared from 40 wt% of silica and 60 wt% of PEG with three different syntheses techniques. As shown in the Fig. 5, it is clear that the STF samples (sample (D) and sample (H)) exhibit shear thickening behavior at lower values of shear rate as compared to samples (I) prepared by simple mixing. Sample (D) has a superior shear thickening behavior as compared to other as-prepared STF samples prepared at same weight fractions of silica and PEG. These results prove that the sonochemical method is an effective synthesis technique for preparation of shear thickening fluid for liquid body armor applications.

The temperature effect on STF samples (samples (D) and sample (H)) were studied by measuring the viscosity changes at 0 °C and 40 °C. Fig. 6a depicts the rheology graph of sample (D) tested at 0 °C. These results show that the sample exhibits a shear thickening behavior at higher shear rate (7/s) as compared to the sample (D) tested at room temperature. It is also noteworthy to mention that the highest value for the sample (D) viscosity at 0 °C is ~66 Pa s which is much less than the maximum viscosity (410 Pa s) value at room temperature. When the temperature increased to 40 °C, the rheology test results show that the sample (D) exhibit shear thinning for a broad range of shear rate (3–30/s) as shown in Fig. 6b. This behavior can be explained as the temperature increases the sample viscosity decreases with the increase of shear rate, then the sample become thinner and have more scattered data for its viscosity until the viscosity become zero Pa s [37,38].

Sample (H) was also tested for its rheological measurements at 0 °C and 40 °C shown in Fig. 7a and b. These results show shear thickening behavior at 0 °C at a shear rate range between 0.3 and 3.5/s and with increase in the viscosity from 6 to 60 Pa s. These results are consistence with the results observed for STF sample (D). Similarly when the sample (H) tested at 40 °C it demonstrated a shear thickening behavior at shear rate 3–50/s. However, the increase in the viscosity is inferior to the sample tested at room temperature. These rheological results at high temperatures clearly suggest that the high temperatures have negative effects on shear thickening fluids as compared to the rheological properties at room temperature.

The actual weight percentages of silica and PEG in STF samples (sample (D) and sample (H)) were estimated using TGA experiments. The TGA graph for STF sample (D) presented in Fig. 8a shows residual weight percentage of 35% of silica at 600 °C. The 5 wt% difference in the weight percentages of added silica (40%) and remaining residual silica (35%) can be explained by the loss of silica nanoparticles during the preparation and TGA experimental error. The TGA graph for sample (H) is presented in Fig. 8b and the residual weight percentage of silica estimated is ~38 wt%. The 2 wt% difference from the added 40 wt% of silica is within the error margin of the instrument and it is acceptable. These results show that there is no loss of silica during the sonochemical synthesis process. Also the graphs show no weight loss at lower temperatures, confirming that the samples do not contain any remaining

Enhancement of Knife Resistance and Interface Shear Stress

Hassan Mahfuz, DeAnna Sewell and Mujib R. Khan

In our previous work with the addition of Gluta we were able to enhance spike resistance of both Kevlar and Spectra based armors almost by a factor of 10 to 230 J-cm^2/g. Correspondingly, improvement in knife performance was just minimal. The system was made of SiO_2+Silane+Gluta reinforced with Spectra. This system will be considered as the reference system for this report. Although knife performance slightly improved with the use of Spectra, the energy level for zero layer penetration remained very low - within 6 J-cm^2/g. A rigorous attempt was undertaken to improve knife resistance using different chemical routes. The idea was to slow down the shearing of fabric by inclusion of nanoparticles into the matrix as well as to the fiber surface. Knife would encounter more frictional resistances cutting through a strongly bonded particle-polymer-fabric system and hence dissipate more energy. Micro-droplet tests were also conducted to determine interface shear stress and associated frictional resistance between the fiber and the matrix.

Enhancing Knife Resistance

A) Introduction of Various other Nanoparticles:

In an attempt to replace silica (SiO2), other nanoparticles such as calcium carbonate ($CaCO_3$), carbon nanotubes (CNT), and titanium dioxide (TiO_2) were used with identical concentration of silica. Results were somewhat mixed; CNT reinforcement increased the spike resistance for zero layer penetration to 150 J-cm^2/g compared to 10 J-cm^2/g of the reference STF-based armor. Values for other two nanoparticles; $CaCO_3$ and TiO_2 fell below at 90 and 110 J-cm^2/g, respectively. The results are shown in Fig.1. Although CNT showed good improvement, the results were lower than what was achieved earlier with silica. Subsequent knife tests did not show any change in knife performance.

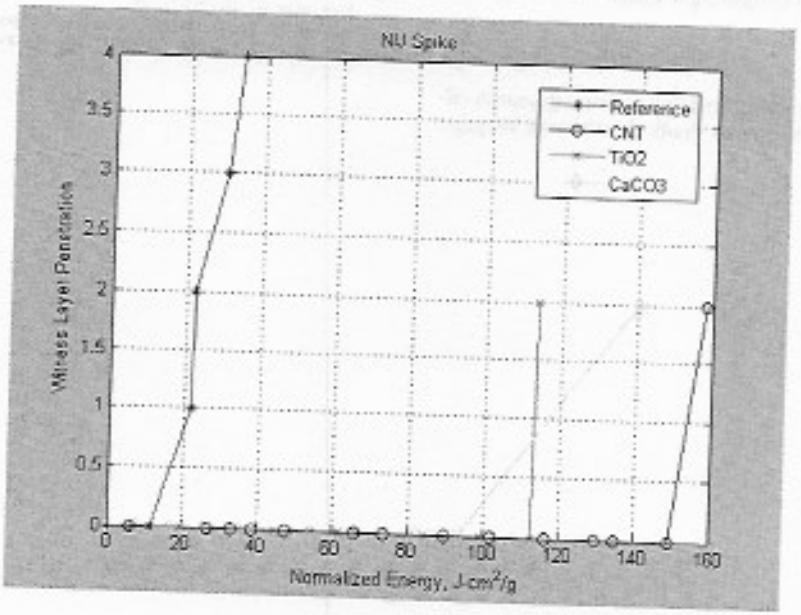


Fig.1: NIJ spike tests with various nanoparticles

quantity of CA300X POSS as the supplier had only a limited stock. This prevented us to have multiple soaking of Spectra with POSS reinforced silane. We strongly believe that multiple soaking with POSS, knife resistance could go beyond that of styrene.

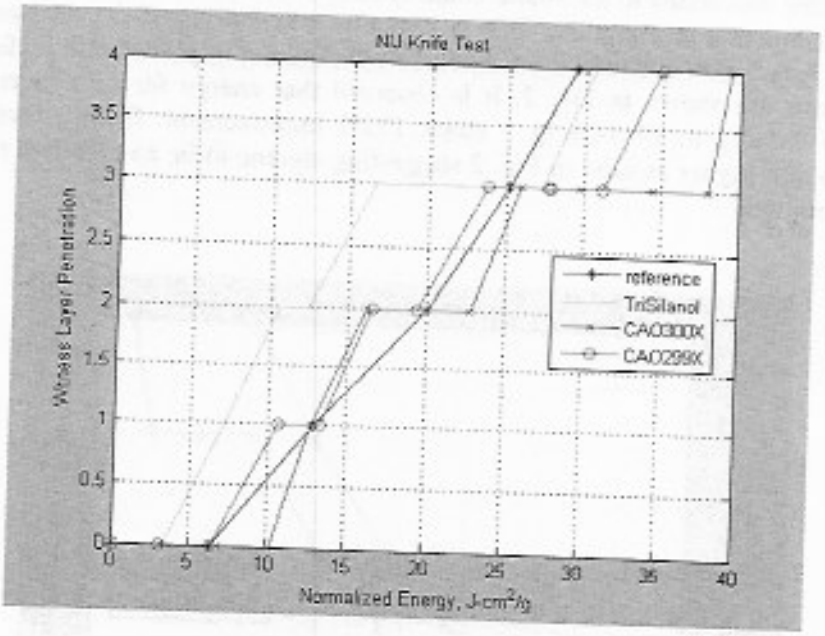


Fig. 3: NIJ knife tests with POSS reinforcement

D) Multiple Soaks with the Reference Solution

The reference solution here is the original SiO_2+Silane+Gluta solution that was used to soak Spectra fibers. To increase the amount of particles adhering to the fiber surface, multiple soaking strategy were taken. After each soak, fabrics were dried and soaked again in a fresh solution, and then dried again. This continued for 2-3 times and the materials were ready for NUJ knife tests. Results are shown in Fig.4. As expected, triple soaking helped improve knife resistance to 20 J-cm^2/g for zero layer penetration – by far the best performance we have seen so far. Soaking beyond three times resulted in excess silica in the panel and thus lowered the energy level.

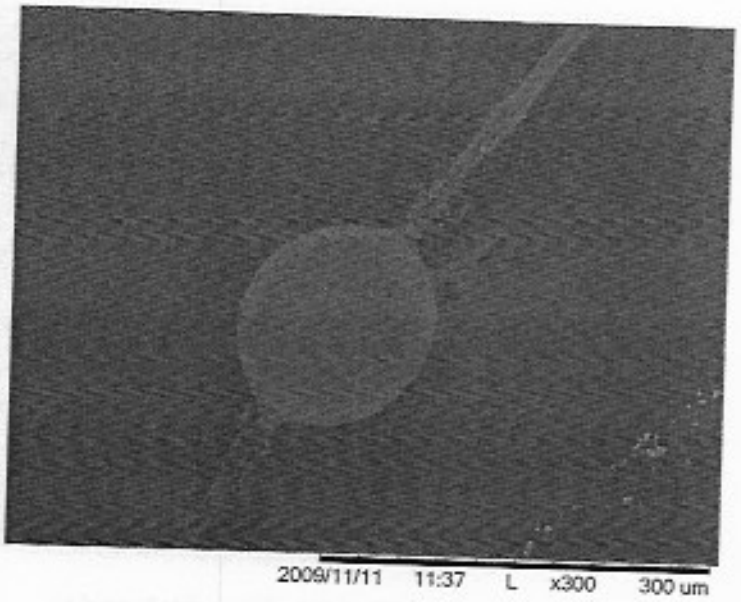


Fig. 5: Microdroplet with embedded fiber

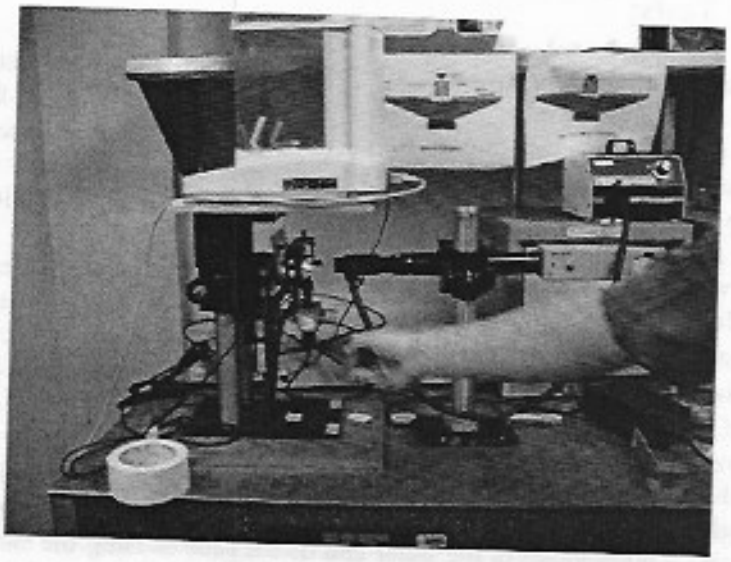


Fig. 6: Micro droplet test set up

The figure indicates a very small force compared to conventional fiber/matrix debonding force. However, we observe a much greater energy absorption in dynamic and static sliding region due to a large amount of friction. This behavior is similar to strain hardening behavior of materials but caused by friction between fiber and particle-polymer mixture in this case. We believe such high friction is responsible to absorb a large amount of energy during spike and knife tests.

Rheol Acta
DOI 10.1007/s00397-010-0463-8

ORIGINAL CONTRIBUTION

Investigating the transient response of a shear thickening fluid using the split Hopkinson pressure bar technique

Amanda S. Lim · Sergey L. Lopatnikov · Norman J. Wagner · John W. Gillespie Jr.

Received: 30 November 2009 / Revised: 1 March 2010 / Accepted: 6 May 2010
© Springer-Verlag 2010

Abstract The split Hopkinson pressure bar (SHPB) technique is implemented to evaluate the transient response of a colloidal suspension exhibiting shear thickening at strain rates and timescales never before explored in a laboratory instrument. These suspensions are shown to exhibit a discontinuous transition from fluid-like (shear thinning) to solid-like (shear thickening) behavior when evaluated using rotational rheometry. The effect of loading rate on this transition time is studied for a particle volume fraction of 0.54 using the SHPB technique. It is shown that the time required for transition to occur decreases logarithmically with loading rate. From these results, we conclude that transition is not triggered by a characteristic shear rate, but rather a critical shear strain is required. Results from SHPB experiments performed up to Peclet numbers of order 10^7 are presented and discussed for 0.50, 0.52, and 0.54 particle volume fraction suspensions.

Keywords Shear thickening · Colloidal dispersion · Squeeze flow · High strain rate · Impact

A. S. Lim · J. W. Gillespie Jr. (✉)
Center for Composite Materials,
Department of Materials Science and Engineering,
University of Delaware, Newark, DE 19716, USA
e-mail: gillespi@udel.edu

S. L. Lopatnikov · J. W. Gillespie Jr.
Center for Composite Materials,
Department of Civil and Environmental Engineering,
University of Delaware, Newark, DE 19716, USA

N. J. Wagner
Center for Composite Materials,
Department of Chemical Engineering,
University of Delaware, Newark, DE 19716, USA

Introduction

The focus of this study is on monodisperse suspensions of colloidal particles, which have been shown to transition rapidly from a fluid-like (Newtonian or shear-thinning) to solid-like state under an increasing applied shear load (Barnes 1989); the micromechanics of shear thickening behavior was first explored over three decades ago (Hoffman 1972).

Shear thickening suspensions appear in many applications, such as paints, cement, and abrasive cleaners (Larson 1999; see also, for example, a recent workshop by Coussot and Wagner 2009), where shear thickening is often undesirable and limits the application. On the other hand and more specific to this research, shear thickening hard-sphere colloidal suspensions have found applications in a variety of fields, including impact resistance (Lee et al. 2003; Tan et al. 2005; Decker et al. 2007) and vibration mitigation (Laun et al. 1991), specifically in composite sandwich structures (Fischer et al. 2006), automotive dampers (Helber et al. 1990), and padding for hip protectors (Robinovitch et al. 1995). As many of these applications are dynamic by nature, understanding the response of shear thickening suspensions under dynamic loading, especially at very high rates, is of importance. However, to date, studies of the dynamics of shear thickening have been limited to timescales typically accessible in commercial rheometers, which is on the order of 10 ms, and at shear rates under 10^5 (Bender and Wagner 1996; O'Brien and Mackay 2000; Lee and Wagner 2003).

From a dynamic standpoint, the time required for this transition to occur and the factors affecting this are critical for many applications, such as in ballistic protection. This time will depend on the microstructural

compression (Kenner 1980; Hoglund and Larsson 1997; Ährström et al. 2002) loading. The squeeze flow SHPB configuration has been validated for Newtonian fluids (Lim et al. 2008a, b) and an analysis is performed to demonstrate the accuracy of the results presented in this paper.

Materials and methods

Suspension preparation

The hard-sphere colloidal suspensions (referred to as shear thickening fluids, STF) evaluated in this study consist of 50%, 52%, and 54% volume fraction (ϕ) silica particles and have been the subject of earlier investigations (Kalman and Wagner 2009). The silica particles (Fig. 1) are nearly monodisperse with a hydrodynamic diameter of 520 nm with less than 10% polydispersity as reported previously. These particles were oven dried and suspended in polyethylene glycol 200 (Alfa Aesar) through a combination of hand mixing and roll mixing for 72 h.

Densities (ρ) of 1.95 g/cc and 1.127 g/cc are reported by the manufacturers for the silica particles and polyethylene glycol 200, respectively. A sound velocity (c) of 1,650 m/s (ρ = 1,120.5 kg/m^3, K = 3.05 GPa) is reported for low molecular weight polyethylene glycols (Sasahara et al. 1998). For silica glasses, a sound velocity of 5,869 m/s is reported (Lynch 1980). To determine the density of the suspension or shear thickening fluid, a rule of ideal mixtures is used (Eq. 1).

$$\rho_{STF} = \phi_s \rho_{silica} + (1 - \phi_s)\,\rho_{PEG} \tag{1}$$

This yields a suspension density of 1.57 g/cc. These material properties will be used in later calculations in the subsection on specimen design.

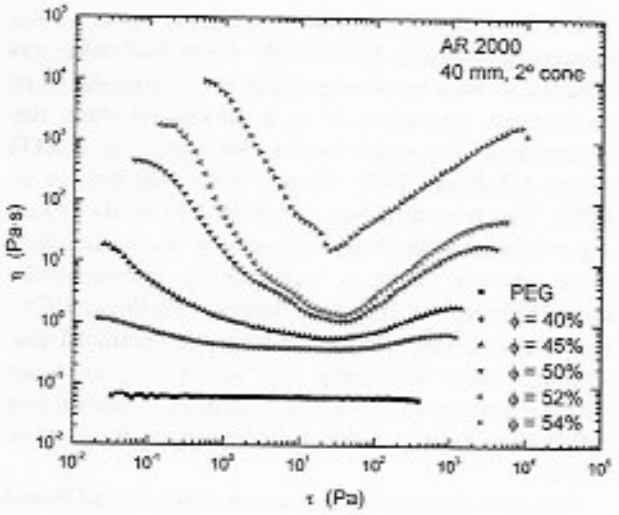


Fig. 2 Steady state shear viscosity of the colloidal dispersions at varying volume fractions and the suspending medium (PEG)

Shear rheology

The steady state shear viscosity of these STFs is plotted along with that for the suspending medium, PEG 200 in Fig. 2. This was measured using an AR-2000 rotational rheometer in the steady-state shear sweep mode using a 40 mm 2° cone and plate with Peltier temperature control at 25°C. These STFs exhibit a shear thinning regime, followed by a strong shear thickening response at relatively low shear rates (1–200 s^{-1}). Note that the point of shear thickening occurs around 3–4 Pa for the most concentrated samples (Fig. 2), and that this behavior is reversible (the data are both ascending and descending curves superimposed). In contrast, the PEG 200 is essentially Newtonian over this range of shear rates.

At lower volume fractions (ϕ < 40%), the suspension exhibits only comparatively weak shear thinning and thickening (Bender and Wagner 1996). As the fo-

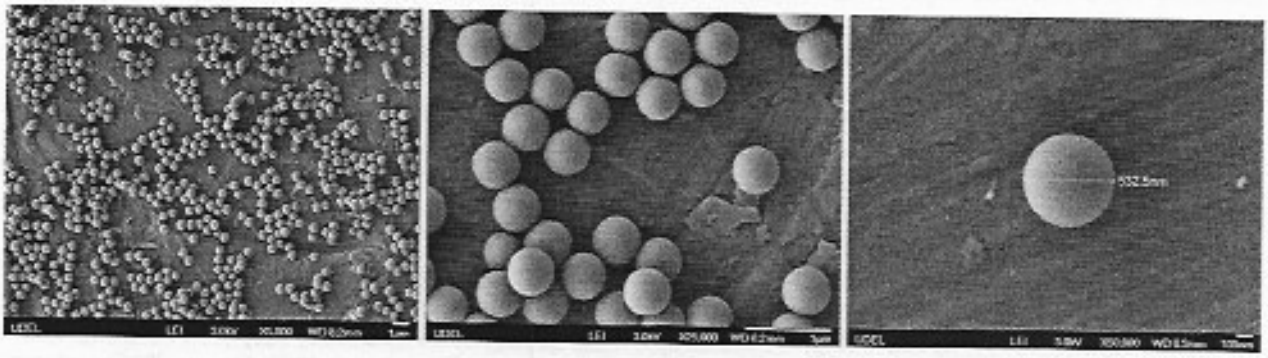


Fig. 1 Silica particles at increasing magnifications

requiring any knowledge of the material properties of the specimen.

$$\dot{\varepsilon} = \frac{C_{0,IB}(-\varepsilon_I + \varepsilon_R) + C_{0,TB}\varepsilon_T}{H_S} \tag{2}$$

$$\sigma = \frac{A_B E_B}{2A_s}(\varepsilon_I + \varepsilon_R + \varepsilon_T) \tag{3}$$

Thus, the compressional stresses, strain rates, and strains are reported here as "engineering" values, namely with reference to the initial sample cross-sectional area (A_S) and thickness (H_S), respectively. This is traditional in the SHPB method (Gama et al. 2004) as well as often employed in polymer squeeze flow testing.

During testing, the suspension is placed at the interface between the incident and transmission bars. The specimen is then covered by a flexible band, which prevents loss of material due to gravity while allowing the specimen to expand radially. The pressure developed by the band has been measured previously by Lim et al. (2009) and was found to be two orders of magnitude lower than pressures associated with the Hopkinson bar experiments performed in this research. Therefore, this band has a negligible effect on measurements made during testing. Experiments are conducted at an average temperature of 22.4 ± 0.4°C. For each experiment, a new specimen is used and the temperature before and after testing is measured.

To demonstrate consistency between experiments, two test results are compared in Fig. 5. The incident bar strain gage signal is plotted for each test with the incident (negative/compressive) and reflected (positive/tensile) pulses marked. The incident pulses are nearly identical (test 2 has a peak stress within 5% of test 1), indicating that these experiments were performed under the same conditions. The reflected pulses are also nearly identical; if experiments were not reproducible, the reflected pulse would vary between the two.

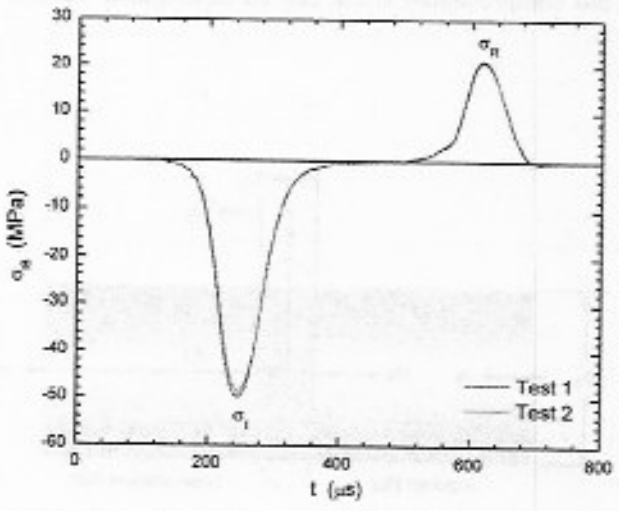


Fig. 5 Incident bar strain gage signals for two experiments performed under identical conditions

Specimen design

Thin specimens (0.55 mm) are used in order to achieve a strong transmitted signal. These specimens are 1,000 times larger than the average particle diameter, ensuring that homogeneous suspension properties are being probed. The specimen radius is kept equal to that of the incident and transmission bars in order to ensure that there is no dispersion due to reflections off the bar ends (Gama 2004).

A specimen may be considered to be in force equilibrium after an initial *ringing up* period (Gray III 2000), which is a function of the material properties and geometry. This is often discussed in terms of the specimen thickness and sound velocity; in fact, a typical estimate is $4t_0$, "where t_0 is the transit time for the leading edge of the pulse traveling through the specimen." (Ravichandran and Subhash 1994; Li and Lambros 1999). A rough estimate of the ringing up time for our material can be calculated with the understanding that, when dealing with a fluid, more complex processes will contribute to equilibrium (Lim et al. 2009). The sound velocity of the suspension is bound by the sound velocity of bulk silica and that of the solvent (c_0 = 1,650–5,869 m/s). A specimen thickness of 0.55 mm yields a ringing up period of 0.37–1.33 μs.

This ringing up time may also be determined experimentally using the homogenization ratio, $R(t)$ (Ravichandran and Subhash 1994), where σ_{IB} and σ_{TB} are the axial stresses at the IB and TB ends of the specimen (Eq. 4).

$$R(t) = \left| \frac{\sigma_{IB} - \sigma_{TB}}{(\sigma_{IB} + \sigma_{TB})/2} \right| \tag{4}$$

This ratio is plotted in Fig. 6 for a typical suspension specimen. The ringing up period is considered complete when the variation between the incident and transmission bar stresses drops below 10%. For the experiment plotted in Fig. 6, this occurs within 50 μs. That this time is larger than predictions based on model elastic materials (which consider only sound travel time) is reasonable given that the rheological behavior of the suspension is viscoelastic. It will be shown that

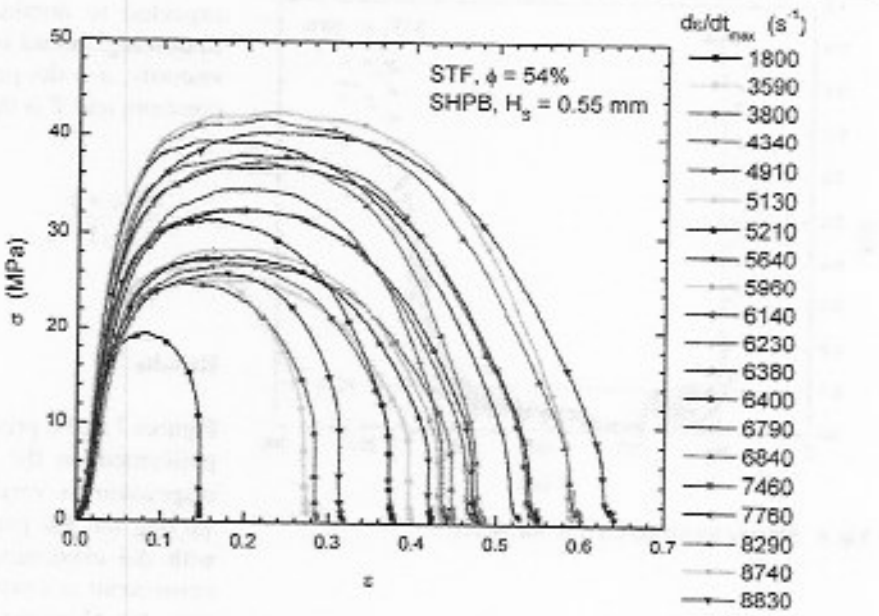


Fig. 7 Stress-strain data for the 54 vol.% suspension obtained via SHPB technique

Fig. 7, are not obviously ordered at higher strain rates. These two representations of the data indicate that both strain rate and strain affect the state of stress of the sample.

To help better understand the specimen's response, Fig. 9 compares the SHPB results for a 54 vol.% suspension with the model calculations for a Newtonian fluid specimen with a viscosity of 15 Pa s under the same test conditions. The calculations use the quasi-static squeeze flow model, which accounts for radial inertia (Kuzma 1967). During loading, the STF undergoes an initial period of deformation marked by an increase in stress with strain rate. At stresses above 2 MPa, the bars decelerate, indicating substantial stiffening within the specimen. After this point (~5 MPa), the STF continues to deform under loading with high resistance. Unloading leads to a higher stress during deceleration with substantial hysteresis. The sample has a much higher stress at the lower shear rates during deceleration. This is in contrast to the Newtonian fluid, which undergoes near linear loading and unloading, with no evidence of stiffening. Behavior of the 0.50 and 0.52 volume fraction silica suspensions is presented and discussed in the Appendix.

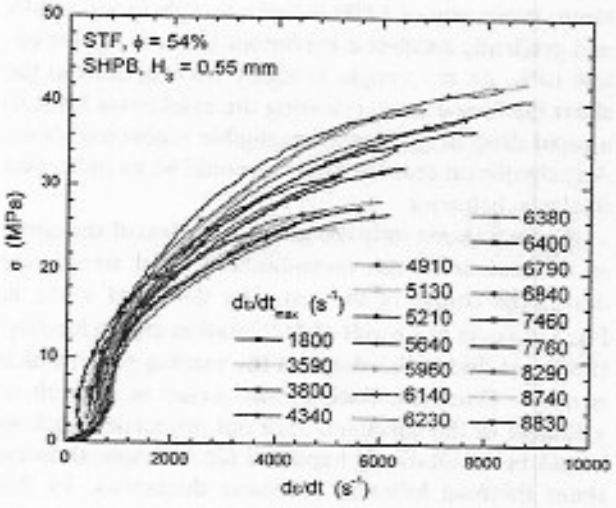


Fig. 8 Loading portion of the stress–strain rate data obtained via SHPB technique

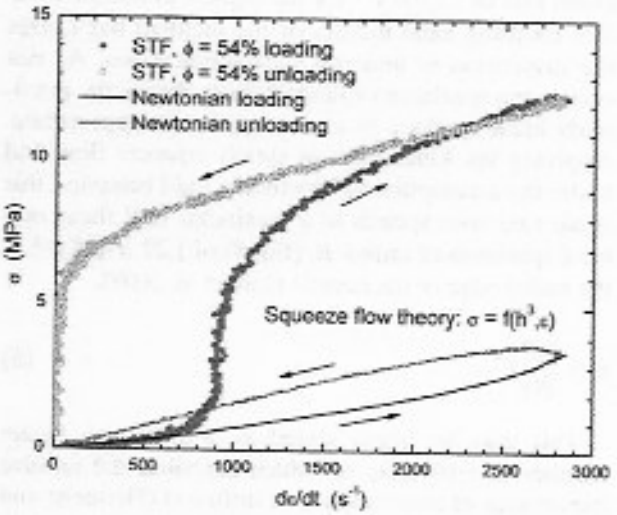


Fig. 9 Comparison of results for a 54% STF with calculations for a 15 Pa s Newtonian fluid

maximum strain rate of each test (Fig. 11). The transition time decreases with increasing strain rate and ranges from 50 to 20 μs. From this plot, it is evident that the transition time decreases exponentially with the maximum compressive strain rate.

Concentration effect

The effect of colloid concentration on the mechanical response of a hard-sphere suspension can be observed by comparing samples at similar conditions. In Fig. 12, the incident bar strain gage signal has been plotted for 50, 52, and 54 vol.% suspension. The incident wave is negative since the loading is compressive while the reflected tensile wave is positive. These experiments all have very similar loading pulses, hence it is appropriate to directly compare them. As expected, the highest concentration suspension exhibits higher stiffness and lower hysteresis than the other two concentrations (Fig. 13a). Interestingly, the suspensions appear to undergo similar loading behavior prior to stiffening (Fig. 13b), but the discontinuous shear thickening sample (54%) exhibits a much sharper rise in stress at the transition than the continuous shear thickening samples of lower volume fraction. That the transition, defined as a decrease in compressive acceleration, appears to begin at approximately the same stress for each sample is consistent with the observations of the steady state rheology in Fig. 2.

The fact that these facets of the mechanical behavior of the STF suspensions can be captured here demonstrates the applicability of the SHPB experimental technique for complex fluid evaluation. It is possible to observe the changes in material response which can occur with a change as small as 2% volume silica, similar to that observed in a rotational rheometer (Fig. 2).

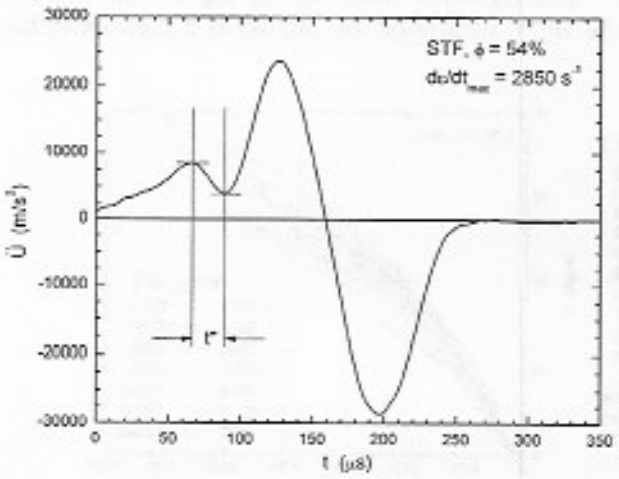


Fig. 12 Acceleration of a 54% silica specimen plotted against time. The plot includes both loading and unloading responses. The time for shear thickening is defined by the indicated transition points

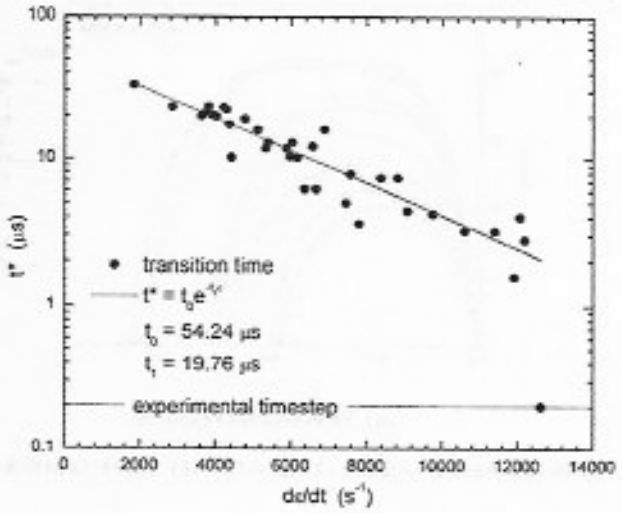


Fig. 13 Transition time for 36 SHPB experiments as a function of strain rate

Discussion

Transition

The results in Fig. 11 indicate that the time required for a STF to transition decreases logarithmically with loading rate. This indicates that a specimen is able to transition to the shear thickened state faster at higher compression rates. This alone is an interesting conclusion, but does not address the issue of whether

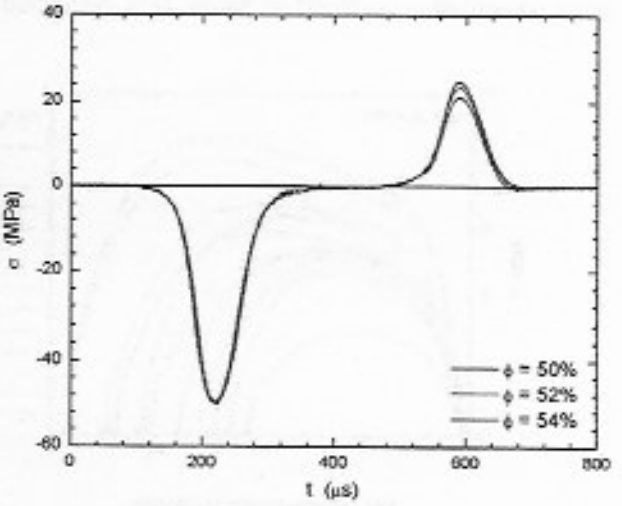


Fig. 14 Incident stress pulses for SHPB experiments on 50, 52 and 54 particle vol.% STFs

slip, this demonstrates that there is a minimum strain required for shear thickening at high Peclet numbers. These results are particularly important for engineering STFs for applications where high rates are applied or short durations are experienced. Further work is required for reduction of the SHPB measurements to material properties as was done previously for Newtonian fluids. For these highly nonlinear fluids, this requires a robust constitutive model and/or independent measurements of the kinematics in the sample during deformation, which is the subject of ongoing research.

Acknowledgements The authors would like to acknowledge Eric D. Wetzel, Ph.D. (Army Research Laboratory), Bazle A. Gama, Ph.D., Joseph M. Deitzel, Ph.D. (University of Delaware Center for Composite Materials), David M. Stepp (Army Research Office), Caroline H. Nam, Ph.D., and Dennis Kalman (University of Delaware Department of Chemical Engineering) for their helpful discussions and contributions to this research. Nick Waite (University of Delaware Department of Electrical Engineering) has also contributed greatly to the development of the current SHPB experimental setup.

Research was sponsored by the US Army Research Office and US Army Research Laboratory and was accomplished under Cooperative Agreement Number #W911NF-05-2-0006. The views and conclusions contained in this document are those of the authors and should not be interpreted as representing the official policies, either expressed or implied, of the Army Research Office, Army Research Laboratory, or the US Government. The US Government is authorized to reproduce and distribute reprints for Government purposes notwithstanding any copyright notation hereon.

Appendix

Examining the results for the lower concentration suspensions (ϕ = 0.50 and 0.52, Figs. 17 and 18), it is observed that these materials experience a weaker loading transition as compared to the more concentrated suspension. However, nonlinear behavior similar to the 0.54 volume fraction suspension is still evident. In Figs. 17 and 18, it can be noted that there is less stiffness in the post-transition material as the highest stresses achieved are generally lower for comparable strain rates.

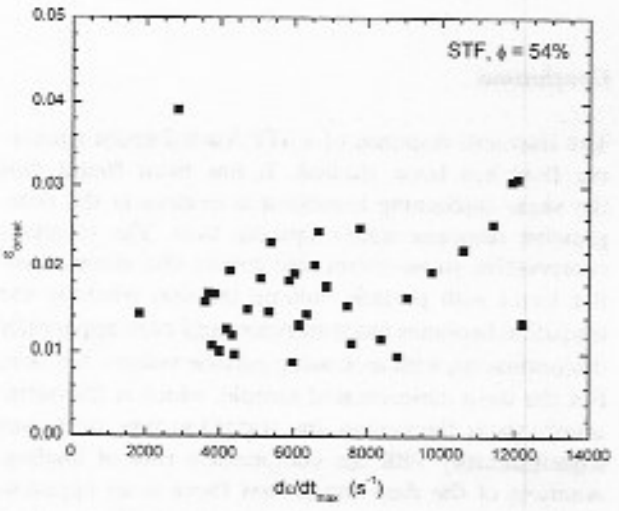


Fig. 17 Compressive strain at the onset of thickening vs. maximum compressive strain rate for the 54 vol.% STF

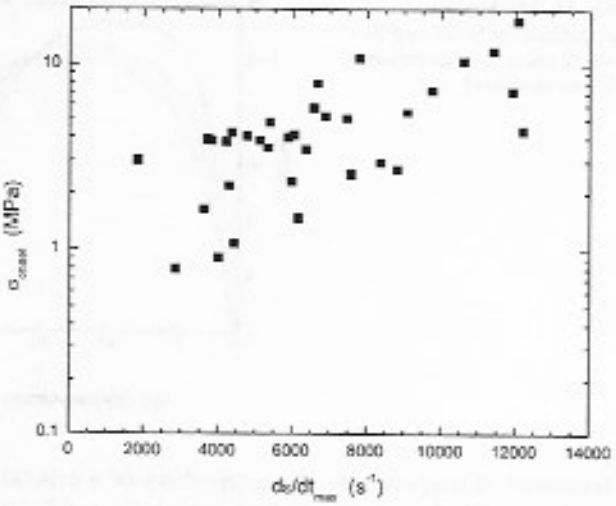


Fig. 18 Compressive stress at the onset of thickening vs. maximum compressive strain rate for the 54 vol.% STF

Due to this lack of discontinuous behavior on the stress–strain rate plot, determining the transition time, as well as the strain at the onset of transition, is very difficult for the case of the 0.50 volume fraction silica suspension. In the case of the 0.52 silica suspension, it is possible to identify the strain at the onset of transition by analyzing the acceleration behavior during loading as seen in Fig. 10. While a decrease in acceleration does not typically occur for this volume fraction, a comparison of the strain at the point of inflection in the acceleration vs. time plot for these experiments has shown that strain at the onset of transition corresponds well with that for the 0.54 silica suspension.

References

Åhrström B, Lindqvist S, Höglund E, Sundin K (2002) Modified split Hopkinson pressure bar method for determination of the dilatation–pressure relationship of lubricants used in elastohydrodynamic lubrication. Proc Inst Mech Eng, Part J J Eng Tribol 216(J2):63–73

Barnes HA (1989) Shear-thickening ("dilatancy") in suspensions of Nonaggregating solid particles dispersed in Newtonian liquids. J Rheol 33(2):329–366

Mechanical Behavior of Silica Nanoparticle-Impregnated Kevlar Fabrics

Zhaoxu Dong, James M. Manimala and C. T. Sun*

School of Aeronautics and Astronautics, Purdue University, West Lafayette, IN 47907-2045, USA

Abstract

This study presents the development of a constitutive model for in-plane mechanical behavior of five styles of plain woven Kevlar fabrics impregnated with silica nanoparticles. The neat fabrics differed in fiber type, yarn count, denier, weave tightness and strength. 4, 8, 16 and 24% by weight of nanoparticles were added to enhance the mechanical properties of the fabric. It was found that fabrics impregnated with nanoparticles exhibit significant improvement in shear stiffness and a slight increase in tensile stiffness along the yarn directions over their neat counterparts. A constitutive model was developed to characterize the nonlinear anisotropic properties of nanoparticle-impregnated fabrics undergoing large shear deformation. The constitutive model parameters were determined based on uniaxial (along yarn directions) and 45^{o} off-axis tension tests. This constitutive model was incorporated in the commercial FEA software ABAQUS through a user-defined material subroutine to simulate various load cases.

Keywords: Kevlar fabric, soft armor, nanoparticle, constitutive model

1. Introduction

Kevlar® fiber is a high modulus, high strength and low density para-aramid synthetic fiber. In comparison to high strength steel, Kevlar has much better strength to weight ratio. It is a good candidate for use as a soft body protection material. The fibers are tightly woven into fabrics and multiple layers of fabrics are used in many soft body armors. The primary goal of soft armor design is to reduce the weight while maintaining the protection level. Hence, weight and performance are the two major criteria that must be balanced in selecting soft body armors.

*Corresponding author. Tel.: +1-765-494-5130; Fax: +1-765-494-0307.

E-mail address: sun@purdue.edu (C. T. Sun).

resistance was observed, and they attributed it to the increase in projectile-fabric and inter-yarn friction.

Many different approaches like simplified orthogonal pin-jointed bars to model yarns, unit cell based models, equivalent homogenized continuum models and detailed 3D models incorporating individual yarns and weave patterns with contact definitions have been used to analyze and model woven fabric material behavior. King et al. (2005) developed a continuum constitutive model for woven fabrics in which the fabric yarn structural configuration is related to the macroscopic deformation through an energy minimization method. Lin et al. (2009) developed a finite element model to predict the shear force versus shear angle response of a plain woven fabric. The fabric was modeled at the yarn scale by assuming yarn behavior to be that of a 3D orthotropic solid. In a recent study by Grujicic et al. (2009), a meso-scale (yarn level) unit cell was developed and its properties were used to model plain woven Kevlar 129 fabric as a continuum surface via a user-defined material subroutine in ABAQUS. The properties of the unit cell were obtained from contact forces and shear response of a solid FEM model of cross yarns in a single unit cell.

In the present study, dry silica nanoparticles were used to reinforce Kevlar fabrics. Unlike the STF-fabric material, these nanoparticle-fabric composites do not contain any fluid and thus minimizes the weight added to neat fabrics. Uniaxial and 45° off-axis tension tests were done to evaluate the in-plane mechanical properties of the fabrics using an MTS servo-hydraulic load frame. It was found that the nanoparticles significantly increased the in-plane shear stiffness, while only slightly influenced the tension behavior along yarn directions. All the tested fabrics exhibited highly nonlinear behavior in shear deformation and large relative rotations between cross yarns. A constitutive model was developed using a method similar to the classical laminated plate theory in conjunction with the incremental deformation approach to characterize the nonlinear anisotropic properties of nanoparticle-impregnated fabrics undergoing large deformation. This model was incorporated in the commercial FEA software ABAQUS via a user-defined material (UMAT) subroutine to simulate the mechanical response of Kevlar fabrics. Validation of the model was done by comparing the numerical results to experimental load displacement curves for a 30° off-axis tension test and static indentation tests. The simulations agree well with the experimental results until the onset of failure.

vacuum mode. The image reveals that silica nanoparticles did not form a uniform coating on the fabric surface but accumulated in the space between fibers. Abrading the surface of the treated fabric dislodges only the particles adhering to the surface but the particles in the inter-fiber spaces remain undisturbed.

2.2 Uniaxial tension tests

To evaluate the yarn direction stiffness of the fabrics, quasistatic uniaxial tension tests were performed on the neat and nanoparticle impregnated fabrics. The fabrics (single layer) with different wt% additions of nanoparticles were tested in both the warp and the weft directions. In order to prepare the specimens for the test, the neat and treated fabrics were cut into a rectangular piece of 25.4 mm in width and 150 mm in length along the yarn directions. Hard end tabs were bonded using epoxy adhesive to both ends leaving a gage length of 102 mm between the tabs. Figure 4(a) shows the dimensions of the final specimen. A 100 KN MTS load frame was used in this test. The crosshead speed was set to 0.1 mm/second. The specimen was aligned and gripped using hydraulic grips during the test. No slippage at the grips was noticed during testing.

2.3 Off-axis tension tests

Picture frame tests are widely used to evaluate the in-plane shear properties of woven fabrics (Mohammed et al. (2000), Peng et al. (2004) and Lomov et al. (2006)). The stress field in the picture frame is usually assumed to be uniform. When shear deformation is small, the fabric does not wrinkle and the uniform stress assumption is reasonable. However, the fabric wrinkles under large shear deformations. This results in nonuniform stress distributions and the accuracy of the test result is not guaranteed.

In view of the foregoing, we employed a 45° off-axis tension (bias extension) test to determine the fabric shear property. The specimen size was the same as that used in the uniaxial tension tests. Figures 4(b) and 4(c) show the initial and deformed configurations. The yarn orientation angle (α) is the acute angle made by the warp direction yarn with the short (25 mm) edge of the specimen as shown in the Figure 4(b). The specimens were cut such that this angle was 45° in the undeformed state. As the warp and weft directions in the fabric are orthogonal to each other initially, this test has a symmetric configuration with respect to both yarn directions. The specimens were tabbed and tested with same experimental setup as the uniaxial tension tests. No slippage at the grips was noticed during testing.

uniaxial response is thus markedly bilinear. The results show that, in general, the weft yarns are stronger than the warp yarns and also display a stiffer response. The addition of nanoparticles to the fabrics seems to increase the uniaxial strength and stiffness only slightly as evidenced by the plots presented in Figure 7. Nonetheless, there are a few observations of interest that present themselves.

Firstly, as the deformation progresses, it is noticed that the width of the specimen remains more or less unchanged. Unlike a homogenous solid, the deformation in fabrics is largely governed by interaction between yarns at the cross over points in the weave. But once the crimp interchange process is complete after the initial loading phase, no transverse yarn pull out is noticed, which indicates that the width of the specimen (distance between outer most axial yarns) remains the same as the initial width of the specimen. This was noted to be the case for all the specimens tested and thus an assumption of negligible lateral contraction is made for the fabric loaded in uniaxial tension.

As the crimp interchange process reduces the yarn waviness in the axial direction while increasing it in the transverse direction, the variation of the overall thickness of the fabric is very small. Variability in the load sensed by individual axial yarns is reduced by ensuring high precision in the specimen fabrication process and alignment and gripping procedure for the test. However one of the factors affecting the scatter in the failure location (apart from any local defects) may be the slight difference in pretension induced due to errors in the aforesaid procedures. Owing to the existence of these conditions in the fabric during the uniaxial tension test, it is reasonable to assume a state of uniform axial stress and strain field. Hence, engineering stress versus strain can be reported using the initial specimen dimensions, which are presented in Figure 7. The thickness of woven fabrics is measured using ASTM D1777-96 standard. The thickness values as quoted by the manufacturer (Table 1) are used to calculate the fabric cross sectional area. The warp and weft fabric strengths as obtained from the tests (Table 2) differ from the manufacturer supplied values given in Table 1. The average difference between measured and supplied value is about 16%. As the manufacturer's test procedure is not supplied with the material data sheet, the variation in the measured strength values is attributed to difference in test methods and conditions. The axial mechanical properties of the fabric are obtained from the test results using a bilinear curve fit. The strength values assume significance only in the context of failure prediction which is not dealt with in the present study.

loading of the fabric. For balanced plain woven Kevlar fabrics with the same yarn count in warp and weft directions, a 45^0 off axis tension (bias extension) test produces a deformation that is symmetric about the longitudinal centerline of the specimen (Figure 4(c)). Distinct shear regions are observed in the specimen during deformation (Harrison et al. (2004), Lebrun et al. (2003)). The central region C as shown in Figure 9 has a pure shear deformation as the yarns experience only rotations relative to each other, while the region A remains undeformed and region B has a shear angle half that in region C. Due to the rotation of the yarns, region C displays large transverse contraction. The length of region C depends on the specimen dimensions and yarn count of the fabric. The load displacement curves show a steep rise after a critical value of displacement is reached in each case. This occurs because as the yarn rotations progress, a limiting angle is reached when adjacent yarns become compactly packed without any inter-yarn spacing. This angle is referred to as the locking angle for fabrics. After the locking angle is reached the shear rigidity of the fabric is driven by the compression of individual yarns in the transverse direction which causes a greater load to be sensed per unit displacement. In the post locking deformation, out of plane wrinkling of the fabrics occur. Failure initiation occurs thereafter by the slipping of the yarns at the interface between shear regions C and B. Unlike the uniaxial tension test, the failure does not occur at a well defined load but progresses gradually as weft and warp yarns slip over each other at cross over points. The oscillatory behavior in the curves at displacements close to failure is due to this phenomenon of yarn sliding at corners. The maximum load is sensed during the yarn sliding phase after which the curve falls rapidly as the two portions of the specimen separate. The failure location was always observed to be at either the upper or lower shear region interfaces. The addition of nanoparticles did not affect the location of failure. However, treated fabrics display a more definite failure load as the enhanced load carrying ability diminishes rapidly once the nanoparticles that lock the relative motion between adjacent yarns are dislodged. This reinforces the inference that the nanoparticles enhance the shear rigidity by increasing the inter-yarn and intra-yarn friction in woven fabrics.

The load displacement plots (Figure 8) demonstrate that substantial enhancement of shear rigidity and strength is achieved by the addition of nanoparticles to the fabric. The effect is greater for coarse weave fabrics which have low rigidity in the neat condition. K745 (the coarsest weave among the five styles) registers a failure load of nearly 26 times that of its neat strength with an addition of 24 % by weight of nanoparticles. In comparison, fine weave fabrics that have

However, an in-plane shear loading can cause very large changes in the angle between the warp and weft yarns due to their relative rotations. This behavior makes the modeling of the fabric as a homogenized continuum rather difficult. In addition, for nanoparticle impregnated fabrics, the effect of the nanoparticles on the mechanical behavior must be included in the constitutive equations.

To simplify this task, we adopt an incremental deformation approach in setting up the constitutive model in conjunction with a procedure that resembles the classical laminated plate theory. As the response of the fabrics is highly non linear, an incremental deformation approach is used. At every increment, the fabric deforms through the interaction of the warp and weft families of yarns. This interaction is simplified by modeling the warp and weft yarns as two separate plies in a composite laminate. Once the incremental constitutive equations are established, they can be implemented as a user defined subroutine in the commercial finite element code ABAQUS/ Standard to perform numerical simulations.

A set of coordinate systems are established as shown in Figure 10. The fabric is assumed to lie in the x-y plane with the warp and weft yarns initially assumed to be oriented at angles α and β respectively to the positive x direction of the global coordinate system x-y. An angle measured anticlockwise from the positive x direction is represented as positive and an angle measured clockwise is represented as negative. As the out of plane thickness of the fabric is very small compared to the specimen in-plane dimensions, an assumption of a state of plane stress is made. For plain woven fabrics the warp and weft directions are orthogonal to each other in the undeformed condition. As the fabric undergoes large shear deformations, the yarns rotate relative to each other and the angle between them in the deformed state (θ) can become much larger or smaller than 90°. Two local coordinate systems, $(x_1\text{-}x_2)_\alpha$ and $(x_1\text{-}x_2)_\beta$ are established for the warp and the weft layers respectively such that the x_1 direction is along the yarn direction in each layer.

At each incremental step, a single layer of Kevlar fabric of thickness T is modeled as the composite of two layers of unidirectional fibers. The effective mechanical properties of each layer are modeled as a two-dimensional orthotropic solid and the fabric is modeled as the laminate consisting of two fiber layers. Considering the warp layer, the incremental stress-strain relations for this layer are formulated in the local coordinate system as

$$\begin{Bmatrix}\Delta\sigma_{xx}\\ \Delta\sigma_{yy}\\ \Delta\sigma_{xy}\end{Bmatrix}=\begin{bmatrix}Q_{11}^{\beta} & Q_{12}^{\beta} & Q_{16}^{\beta}\\ Q_{12}^{\beta} & Q_{22}^{\beta} & Q_{26}^{\beta}\\ Q_{16}^{\beta} & Q_{26}^{\beta} & Q_{66}^{\beta}\end{bmatrix}\begin{Bmatrix}\Delta\varepsilon_{xx}\\ \Delta\varepsilon_{yy}\\ \Delta\gamma_{xy}\end{Bmatrix}=\left[Q^{\beta}\right]\begin{Bmatrix}\Delta\varepsilon_{xx}\\ \Delta\varepsilon_{yy}\\ \Delta\gamma_{xy}\end{Bmatrix} \tag{5}$$

The superscript β denotes the weft layer and the reduced stiffnesses for the weft layer, Q_{ij}^{β} are given by

$$\begin{aligned}
Q_{11}^{\beta} &= E_1^{\beta}\cos^4\beta + 4G_{12}^{\beta}\sin^2\beta\cos^2\beta + E_2^{\alpha}\sin^4\beta\\
Q_{12}^{\beta} &= \left(E_1^{\beta} + E_2^{\beta} - 4G_{12}^{\beta}\right)\sin^2\beta\cos^2\beta\\
Q_{22}^{\beta} &= E_1^{\beta}\sin^4\beta + 4G_{12}^{\beta}\sin^2\beta\cos^2\beta + E_2^{\beta}\cos^4\beta\\
Q_{16}^{\beta} &= \left(E_1^{\beta} - 2G_{12}^{\beta}\right)\sin\beta\cos^3\beta - \left(E_2^{\beta} - 2G_{12}^{\beta}\right)\sin^3\beta\cos\beta\\
Q_{26}^{\beta} &= \left(E_1^{\beta} - 2G_{12}^{\beta}\right)\sin^3\beta\cos\beta - \left(E_2^{\beta} - 2G_{12}^{\beta}\right)\sin\beta\cos^3\beta\\
Q_{66}^{\beta} &= \left(E_1^{\beta} + E_2^{\beta} - 2G_{12}^{\beta}\right)\sin^2\beta\cos^2\beta + G_{12}^{\beta}\left(\sin^4\beta + \cos^4\beta\right)
\end{aligned} \tag{6}$$

The warp and weft layers exist in an interwoven state in the actual fabric and hence to simplify the formulation, we assume that both layers occupy the same space and have the same thickness *(T)* which is the thickness of one fabric layer. This thickness is set to be constant over the fabric undergoing large deformation. To be consistent, material properties for the warp and weft layers are defined using the thickness. Thus, the stiffness matrix for the fabric is obtained as

$$[Q]=\left[Q^{\alpha}\right]+\left[Q^{\beta}\right] \tag{7}$$

Equation (7) provides the stiffness matrix for a single layer of fabric which is dependent on a total of six unknown material parameters – three each for warp and weft yarn directions. For each layer, the moduli E_1, E_2 and G_{12} are calibrated from the uniaxial and off-axis tension tests. These moduli must reflect the variation in yarn spacing under large deformations due to relative rotation of warp and weft yarns. True strain and true stress are used in the ABAQUS incremental formulation. In the following discussion, neat Kevlar K706 style fabric will be used as an example to illustrate the procedure for obtaining the material parameters. The same procedure is followed for other styles of neat and treated fabrics.

The uniaxial tension tests in the warp and weft directions display a bilinear trend. Hence, a simple bilinear function was used to approximate the tangent longitudinal moduli E_1^{α} and E_1^{β} in the warp and weft directions from these stress-strain curves. In the uniaxial tension tests, relative yarn rotations do not occur and thus the yarn spacing remains unchanged. However, when the fabric undergoes shear deformations, yarn rotations induce a change in the tangent longitudinal

causes the yarn spacing parameter to decrease. Thus, the tangent longitudinal moduli which are inversely proportional to the yarn spacing parameters increase as the yarn spacing reduces. This reflects the phenomenon of increase in yarn direction moduli due to increase in friction between adjacent yarns as they become closely packed.

The transverse moduli and the shear modulus are estimated from the 45° off axis tension tests. The mechanism by which the fabric resists shear loads transitions from one predominantly due to rotation of yarns to one due to the transverse compression of adjacent yarns as the relative angle between the yarns approaches the locking angle. Hence, the shear rigidity is very low during the initial phase of the deformation. Once the locking angle is reached, the yarns become closely packed and further deformation is resisted by compression of yarns in the transverse direction and the occurrence of out of plane wrinkling. We introduce this effect into the constitutive relations by assuming that the shear modulus (which is attributed to the initial yarn rotations) to be constant and that the highly non linear behavior at higher displacements are caused by variation in the transverse moduli. The load-displacement curves for the 45° off axis tension test can be converted to an equivalent shear stress-shear angle curve using the kinematic relations for an equivalent picture frame test (Milani et al. (2009)). Comparisons show that both these curves have nearly the same slope at low values of displacement/ strain. Under these assumptions, the shear modulus is estimated from the initial slope of the load-displacement curves from off axis tension tests. The individual shear moduli for the warp and weft layers are indistinguishable. Both G_{12}^{α} and G_{12}^{β} are assumed to be equal and to be the same as that of a single layer of fabric. For neat K706, the shear modulus is calculated from the initial slope of the curve as

$$G_{12}^{\alpha} = G_{12}^{\beta} = G_{12} = 0.4\ MPa \tag{12}$$

The parameters E_2^{α} and E_2^{β} are obtained from the load-displacement curves using a non linear fitting function which depends on the yarn spacing parameters. When the cross yarns undergo large rotation, the parallel yarns are packed together. The stresses in transverse direction prevent the parallel yarns from being too close to each other under large shear deformation. The tangent transverse moduli E_2^{α} and E_2^{β} could be calculate from these transverse stresses. Since both E_2^{α} and E_2^{β} attribute to prevent the further yarn rotation, we assume they are the same nonlinear function in terms of non-dimensional yarn spacing L_{α} and L_{β}. The form of the fitting

experimental and numerical indentor load-displacement curves is presented in Figure 14. The numerical simulations fit the experimental data very well until failure of the fabric begins due to the slipping of yarns at the corners. Since this model does not account for damage, the simulation starts to deviate from the experimental results at large loads.

6. Conclusions

In-plane mechanical properties of five styles of Kevlar fabrics were investigated to show the difference between the neat fabric and the silica nanoparticle impregnated fabrics. The nanoparticles impart substantial increase to the in-plane shear rigidity. When off-axis load is applied, nanoparticle impregnated fabrics sustained higher failure loads. SEM images reveal that the nanoparticles are lodged in the inter-yarn and inter-fiber spaces in the fabric. This increases the friction between adjacent and cross yarns thereby augmenting the fabric's resistance to applied loads.

A two dimensional homogenized continuum constitutive model was developed to characterize the nonlinear anisotropic material properties of the neat and nanoparticle impregnated fabrics under large shear deformation. The material parameters required in this model were obtained from uniaxial tension and 45° off-axis tension tests. The constitutive model was interfaced with the commercial finite element code ABAQUS via a user defined material subroutine (UMAT). Validation of the model was done by simulating a 30° off-axis tension test and a static indentation test. The simulated load-displacement curves were found to agree very well with the experimental data. This model can be used to predict the load deflection behavior of neat and nanoparticle impregnated plain woven Kevlar fabrics with good accuracy.

Acknowledgement

This work was supported by an ARO grant W911NF-05-2-0006. Dr. David Stepp was the program manager. We also wish to thank Dr. Eric Wetzel who provided the Kevlar fabrics used in this study.

Technology, **64** (2004), 11-21.

M.N. Raftenberg and T.J. Mulkern, "Quasi-Static uniaxial tension characteristics of plain-woven Kevlar KM2 fabric", *Army Research Laboratory-Technical Report-2891*, (2002).

V.B.C. Tan, T.E. Tay and W.K. Teo, "Strengthening fabric armour with silica colloidal suspensions", *International Journal of Solids and Structures*, **42**:5-6 (2005), 1561-1576.

Table 1: Manufacturer's product data of five styles of plain woven Kevlar fabrics

Fabric style	K310	K706	K720	K745	K779
Fiber type	Comfort	KM-2	129	29	159
Fiber modulus (GPa)	87.0	80.0	99.7	73.0	97.2
Yarn size (Denier)	400	600	1420	3000	200
Weight (g/m^2)	122	180	258	475	132
Warp count (Yarns/in)	35.5	34	20	17	70
Weft count (Yarns/in)	35.5	34	20	17	70
Warp Strength (lbs/in)	530	775	978	1600	385
Weft Strength (lbs/in)	530	880	992	1800	530
Thickness (mm)	0.18	0.23	0.36	0.61	0.18

Table 2: Neat fabric weights and strengths measured in this study

Fabric style	K310	K706	K720	K745	K779
Weight (g/m^2)	127	178	254	435	127
Warp Strength (lbs/in)	630	760	1220	1770	390
Weft Strength (lbs/in)	730	970	1290	1910	670

Caption of Figures

Figure 1: Optical images of five styles of plain woven Kevlar fabrics. (The image size for all the fabrics are 6.4 x 6.4 mm. The true color of the fabrics was bright yellow. They were post-processed to black and white format to enhance the contrast.)

Figure 2: SEM image of K706 fabric with 24 wt% silica nanoparticles

Figure 3: Identifying warp and weft yarns in the fabric – Warp yarns are wavier than weft yarns

Figure 4: Diagram of tension test specimen: (a) Uniaxial tension, (b) Off axis tension (initial configuration) and (c) Off axis tension (deformed configuration)

Figure 5: Schematic diagram of static indentation test

Figure 6: Indentation test on neat K706

Figure 7: Engineering stress versus strain curves from uniaxial tension tests for five styles of Kevlar fabrics with different wt% of nanoparticle addition

Figure 8: Load versus displacement curves from 45° off axis tension tests for five styles of Kevlar fabrics with different wt% addition of nanoparticles

Figure 9: Shear regions in a 45° off axis tension test – schematic diagram and actual deformation.

Figure 10: Coordinate systems

Figure 11: Yarn spacing parameters – initial and deformed configurations

Figure 12: Experimental and numerical load-displacement curves for a (a) 45° and (b) 30° off axis tension test using neat K706 style fabric

Figure 13: A snapshot of the deformation in a 30° off axis tension test using neat K706 style fabric at a grip displacement of 18mm – (a) experimental and (b) simulations

Figure 14: Comparison of the experimental and numerical load versus displacement curves from a static indentation test on 45° neat K706 style fabric

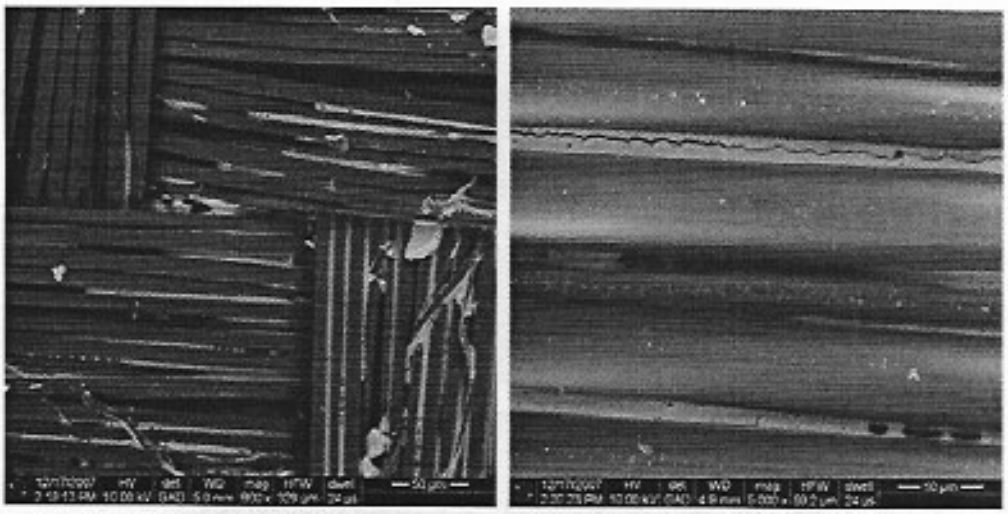


Figure 2: SEM image of K706 fabric with 24 wt% silica nanoparticles

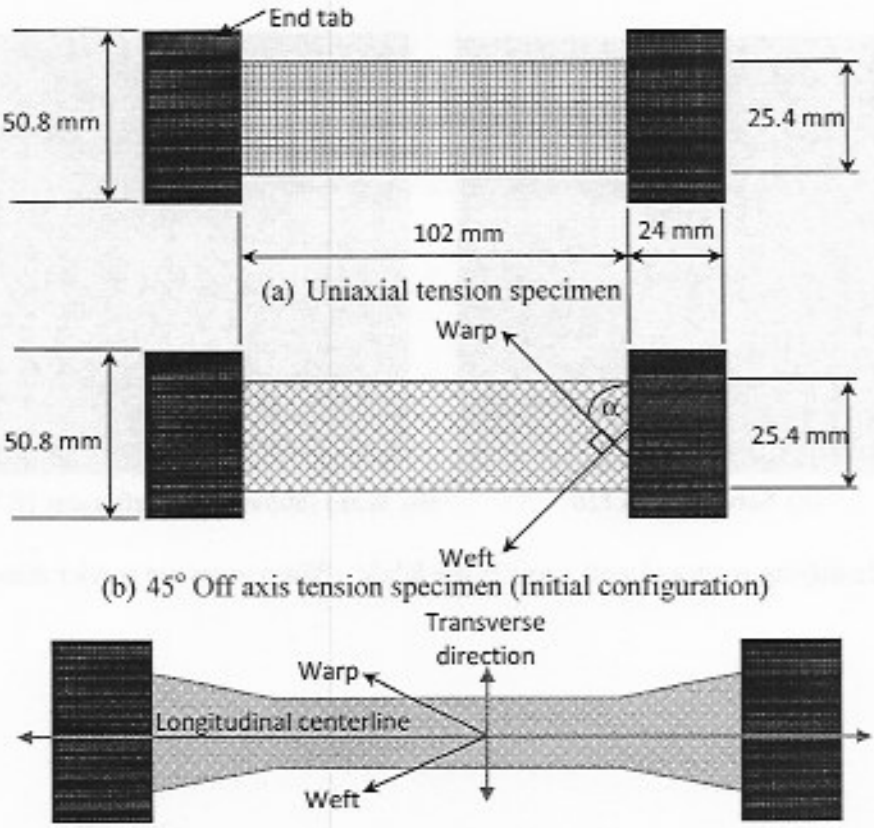


Figure 4: Diagram of tension test specimen: (a) Uniaxial tension, (b) Off axis tension (initial configuration) and (c) Off axis tension (deformed configuration)

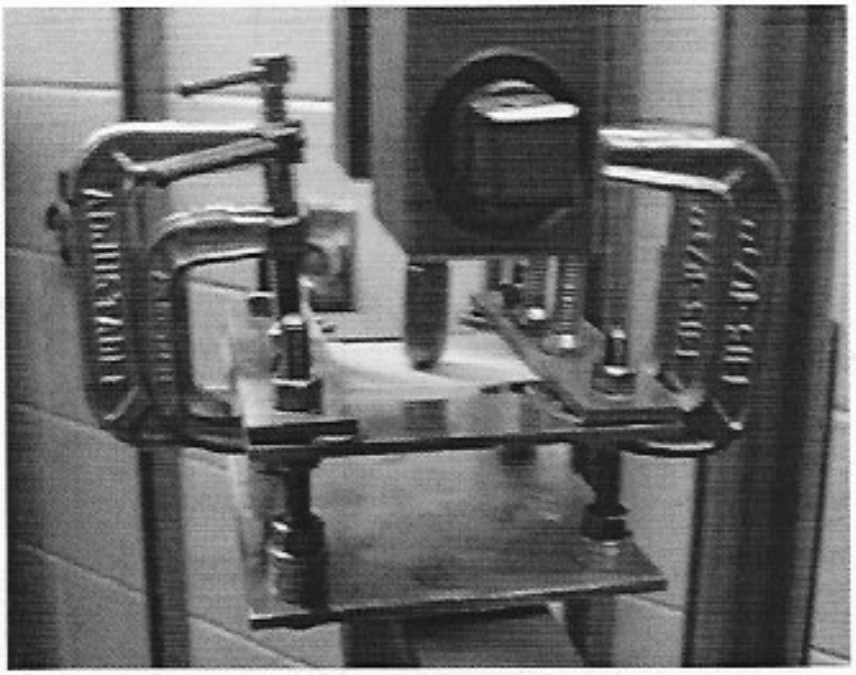


Figure 6: Indentation test on neat K706

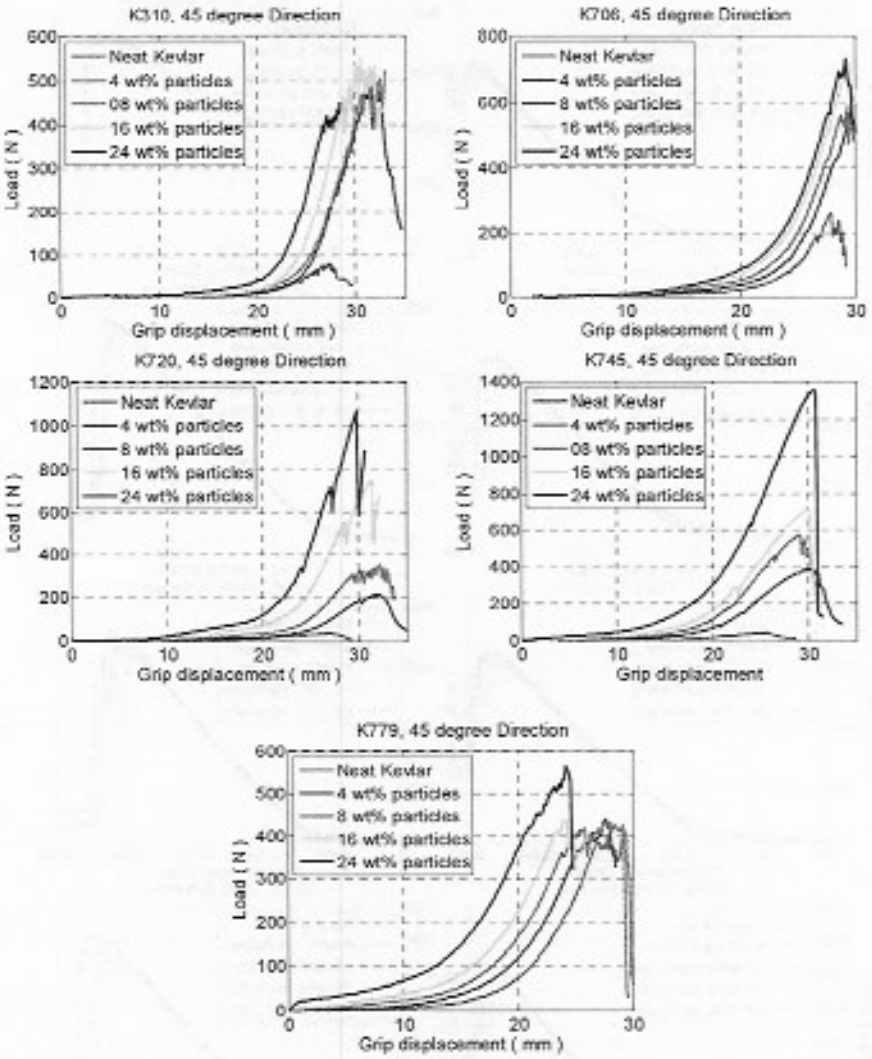
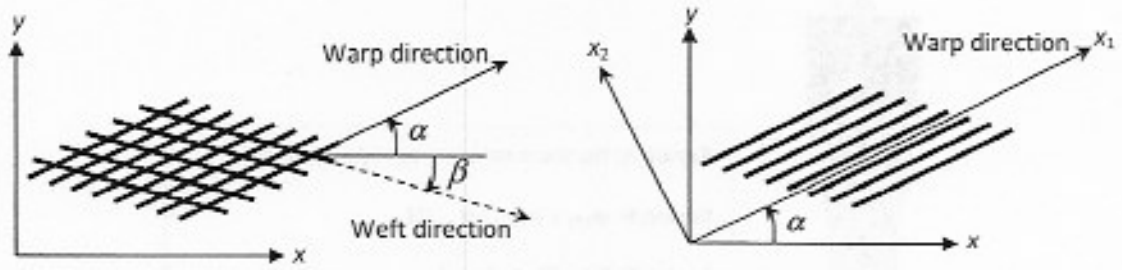


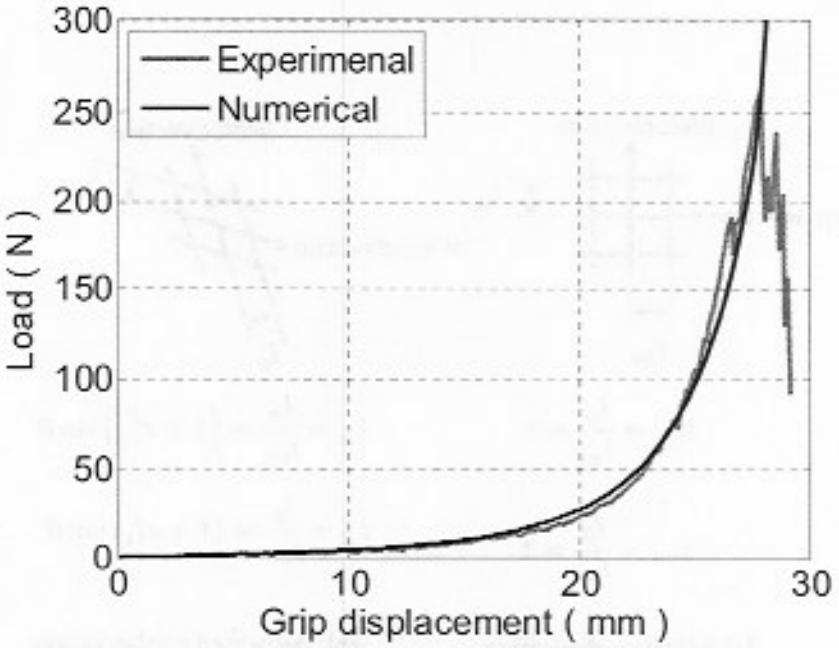
Figure 8: Load versus displacement curves from 45° off axis tension tests for five styles of Kevlar fabrics with different wt% addition of nanoparticles



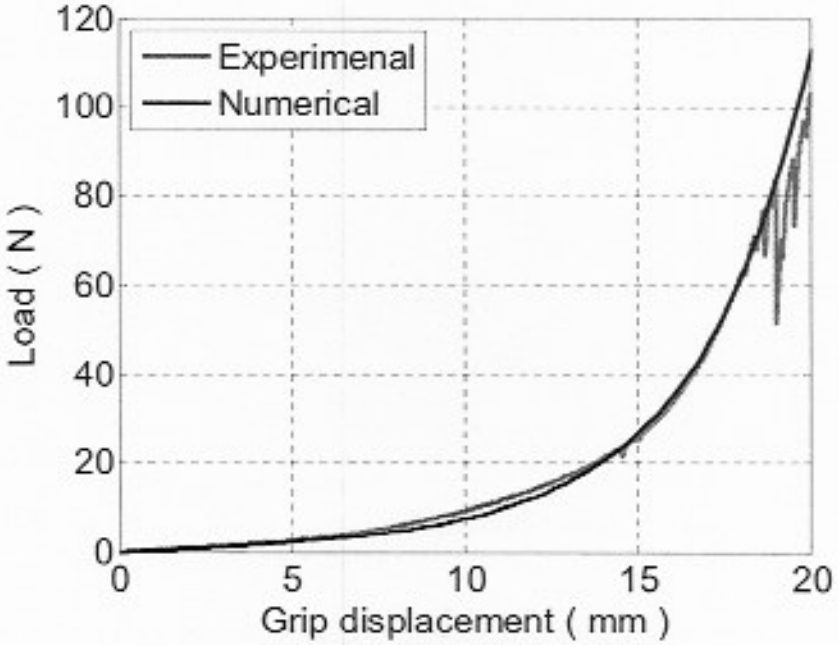
(a) Global coordinate system (x-y) and yarn orientations

(b) Local coordinate system (x_1-x_2) for the warp layer

Figure 10: Coordinate systems

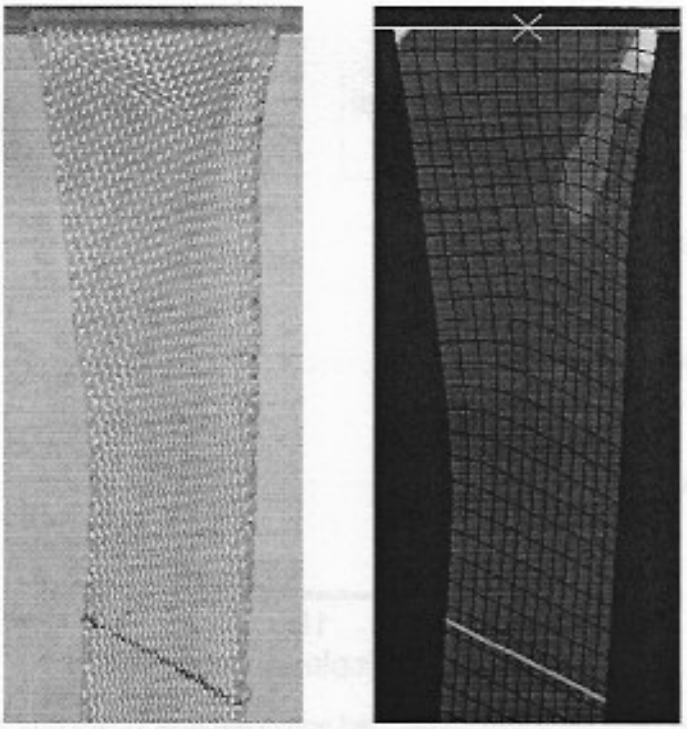


(a) 45° off axis tension test (neat K706)



(b) 30° off axis tension test (neat K706)

Figure 12: Experimental and numerical load-displacement curves for a (a) 45° and (b) 30° off axis tension test using neat K706 style fabric



(a) Experimental (b) Simulation

Figure 13: A snapshot of the deformation in a 30° off axis tension test using neat K706 style fabric at a grip displacement of 18mm – (a) experimental and (b) simulations